

https://dspace.org/

Numerical investigation of wind turbine wake characteristics using a coupled CFDCSD method considering blade and tower flexibility

D Zhang; Z Liu; Weipeng Li; Ling Cheng; Gang Hu

ELSEVIER SCIENCE BV
https://hdl.handle.net/10539/41951
WOS

Downloaded from a DSpace repository. https://dspace.org/

Journal of Wind Engineering & Industrial Aerodynamics 244 (2024) 105625

Contents lists available at ScienceDirect

Journal of Wind Engineering & Industrial Aerodynamics

journal homepage: www.elsevier.com/locate/jweia

Numerical investigation of wind turbine wake characteristics using a coupled CFD-CSD method considering blade and tower flexibility

Dongqin Zhang [a], Zhenqing Liu [b,*], Weipeng Li [b], Ling Cheng [c], Gang Hu [a]

[a] School of Civil and Environmental Engineering, Harbin Institute of Technology, Shenzhen, 518055, China
[b] School of Civil and Hydraulic Engineering, Huazhong University of Science and Technology, Wuhan, Hubei, 430074, China
[c] School of Electrical and Information Engineering, University of the Witwatersrand, Johannesburg, 2000, South Africa

ARTICLE INFO

Keywords:
wake characteristics
Wind turbine
Coupled CFD-CSD
LES
blade and tower flexibility
Inflow conditions

ABSTRACT

With the increase in wind turbine sizes, careful investigation into wind turbine wake effect is crucial for operational safety. This study proposes a two-way fluid-structure interaction (FSI) model combining large eddy simulation (LES) and computational structural dynamics (CSD) to investigate wind turbine wake characteristics. Examining the effect of blade and tower flexibility and inflow conditions, the study reveals negligible influence of blade and tower flexibility on mean velocity deficit under both inflow conditions. However, they significantly impact turbulence intensity under uniform inflow condition. The tower motion produces a maximum increase of approximately 45% while the blade flap-wise motion has the second-largest impact, increasing the maximum turbulence intensity by approximately 33% when compared with the fully rigid case. Additionally, the study quantitatively examines wake vortex inclination based on the inclination angle of the second-circle wake vortex structure. Finally, the study concludes that the streamline near the blade tip follows the blade surface, while the flow separation occurs near the blade root, generating two vortices on the suction side. As the tower motion is considered, the larger vortex exhibits alternate vortex shedding while the smaller vortex remains stable in both uniform and turbulent winds.

1. Introduction

Wind power is increasingly recognized as a promising renewable energy source, owing to its cleanliness and cost competitiveness. The World Wind Energy Association (WWEA) statistical data for 2022 (GWEC, 2022), as shown in Fig. 1, demonstrates a rapid development of the global wind power industry. Over the past two decades, the installed capacity of wind turbines has continuously expanded. The market for wind power witnessed the addition of 97.3 GW of new capacity in 2021, leading to a total global capacity of 840 GW. To enhance power generation and reduce investment costs, wind farms install dozens or even hundreds of wind turbines. However, the flow of winds passing over an upstream wind turbine creates turbulence and a slower wind speed in the area downstream of the turbine, a phenomenon known as the wake effect. Mitigating the wake effect is critical in maximizing the efficiency of wind farms and minimizing their impact on the environment and surrounding communities.

Extensive research has been conducted to investigate the wake characteristics of wind turbine, which fall into four categories: theoretical methods, machine learning, numerical simulations, and experiments. Theoretical wake models have been widely used for wind farm layout optimization and active yaw control to improve efficiency (Liu et al., 2021a, 2021b). Traditionally, these models rely on mass and momentum equations that describe the flow of air within the operating region of wind turbine and have evolved to include the top-hat (Katic et al., 1986; Jensen, 1983), Gaussian (Bastankhah and Porté-Agel, 2014; Ishihara and Qian, 2018), and cosine-shaped (Tian et al., 2015; Zhang et al., 2020) wake models, as well as three-dimensional (Sun and Yang, 2018; Gao et al., 2020) and full wake models (Ge et al., 2019; Keane, 2021). Zhang et al. (2022); Lopes et al. (2022); Zhang et al. (2023) evaluated the accuracy of hundreds of wind turbine wake models. In recent years, researchers (Ti et al., 2020; Zhang and Zhao, 2020; Yang and Deng, 2023) proposed the machine learning-based wake models to evaluate the velocity deficit caused by wind. Additionally, numerical simulations are commonly adopted to explore wake characteristics and the flow dynamics in the wake region by actuator disc modelling (ADM) (Qian and Ishihara, 2019), the actuator line modelling (ALM) (D. Zhang et al., 2022), and full rotor geometry (FRG) method (Abdelsalam et al.,

* Corresponding author.
E-mail address: liuzhenqing@hust.edu.cn (Z. Liu).

https://doi.org/10.1016/j.jweia.2023.105625
Received 29 May 2023; Received in revised form 1 December 2023; Accepted 1 December 2023
Available online 14 December 2023
0167-6105/© 2023 Elsevier Ltd. All rights reserved.

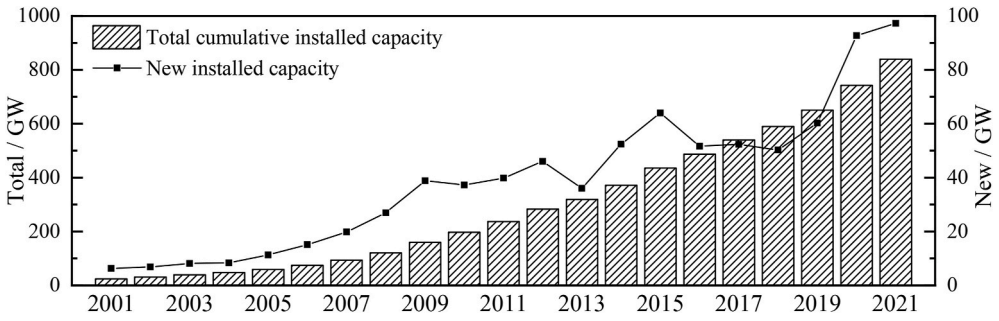

Fig. 1. The annual accumulated installed capacity all over the world.

2014; Cai et al., 2023; Fu et al., 2023; Ye et al., 2023). Experiment is also conducted to study wake characteristics due to its accuracy, including laboratorial experiments (Uchida and Gagnon, 2022; Huang et al., 2022) and field tests (Gao et al., 2020). Overall, research into wind turbine wakes has yielded a diverse array of methodologies and findings that continue to make valuable contributions to the field.

As wind turbines continue to grow in size, it becomes crucial to examine the effect of flexible blades on wake characteristics. Table 1 summarized the FSI simulations of wind turbines conducted in the last few decades. For one-way FSI simulations, the blade element momentum (BEM) theory is widely used in commercial software to simulate wind turbine aerodynamics. The structural dynamics are typically investigated using modal shape (Modal), multibody dynamics (MBD), and finite element method (FEM). In two-way FSI simulations, the blades are either directly modeled using FRG or simulated using the ALM. However, in previous studies, blades were modeled directly using Reynolds-averaged Navier-Stokes (RANS) or delayed detached eddy simulation (DDES), which have limited accuracy. Li et al. (2020, 2023) studied aerodynamic and aeroelastic characteristics of flexible wind turbine blades under periodic unsteady winds using BEM and FEM. Recently, Li et al. (2015) combined the CFD and MBD to study the wind turbine wake characteristics, concluding that velocities in the wake region under turbulent winds induced by both rigid and flexible blades are similar. Della Posta et al. (2022) compared streamwise velocities in the wake region obtained through one-way and two-way FSI analysis and found that the difference can be negligible. Leng et al. (2023) proposed a FSI model based on flexible MBD and LES to investigate wake velocity and found that a large velocity fluctuation occurs near the blade tip if a rigid blade is used, while this is eliminated if flexible blades are used. Xu et al. (2023) used a two-way FSI model to investigate the floating offshore wind turbine (FOWT) wake behaviors under atmospheric boundary layer (ABL) inflows. In the far wake region, the offset of the wake center from the hub center has been observed which is beneficial to downstream wind turbines. In addition, they also found that the wake characteristics including the velocity deficit and the turbulence intensity in the wake region for the FOWT and fixed-bottom wind turbine are similar. Muscari et al. (2023) examined the influence of blade flexibility on wake characteristics and concluded that the differences between wake flows with rigid and flexible blades are minor. While previous studies have shown that the difference of mean wind velocity in the wake region between rigid and flexible blades is small, the effect of every flexible component has not yet been systematically discussed, and the impact of blade and tower flexibility on added turbulence intensity has not been thoroughly evaluated. Further research is needed in these areas to better understand the behavior of wind turbine wakes.

Additionally, it is critical to examine the effects of inflow wind conditions on wake characteristics. The atmospheric turbulence effects have been investigated by ADM (Porté-Agel et al., 2011; Wu and

Table 1
Summary of FSI analysis of wind turbine.

	Developer	Aerodynamics	Structural dynamics	Structures
One-way FSI	FAST (Jonkman et al., 2005)	BEM	Modal, MBD	Blade + tower
	HAWC2 (Larsen and Hansen, 2007)	BEM	MBD, FEM	Blade + tower
	GH Bladed (Bossanyi, 2003)	BEM	Modal, FEM	Blade + tower
	ADAMS/WT (ElliotT and Wright, 1994)	BEM	MBD	Blade + tower
	SIMPACK/Wind (Dassault Systems, 2009)	BEM	MBD	Blade + tower
	PHATAS (Lindenburg, 2018)	BEM	MBD	Blade + tower
	FLEX5 (Øye, 1999)	BEM	Modal, FEM	Blade + tower
	BhawC (Couturier and Skjoldan, 2018)	BEM	MBD, FEM	Blade + tower
Two-way FSI	Carrión et al. (2014)	FGR + RANS	Modal	Blade + tower
	Yu and Kwon (2014)	FGR + RANS	FEM	Blade
	Li et al. (2015)	FGR + DDES	MBD	Blade + tower
	Wang et al. (2016)	FGR + RANS	FEM	Blade
	Lee et al. (2017)	FGR + RANS	FEM	Blade + tower
	Dose et al. (2018)	FGR + URANS	FEM	Blade
	Liu et al. (2019); Liu and Xiao (2019)	FGR + RANS	MBD	Blade
	Sayed et al. (2019)	FGR + RANS	FEM	Blade
	Santo et al. (2019)	FGR + RANS	FEM	Blade
	Lee and Kwon (2020)	FGR + RANS	FEM	Blade
	Thangavelu et al. (2021)	FGR + RANS	FEM	Blade
	Della Posta et al. (2022)	ALM + LES	Modal	Blade + tower
	Leng et al. (2023)	ALM + LES	MBD	Blade
	Yassen et al. (2023)	FGR + RANS	FEM	Blade
	Li et al. (2020, 2023)	BEM	FEM	Blade + tower
	Zhang et al. (2023)	BEM	Modal	Blade + tower
	Xu et al. (2023)	ALM + LES	MBD	Blade + tower
	Muscari et al. (2023)	ALM + LES	Modal	Blade
	Proposed	**FGR + LES**	**Modal**	**Blade + tower**

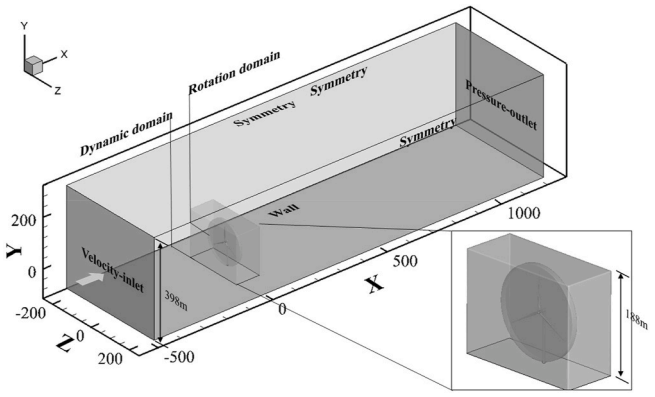

Fig. 2. Configurations of the computational domain and boundary conditions.

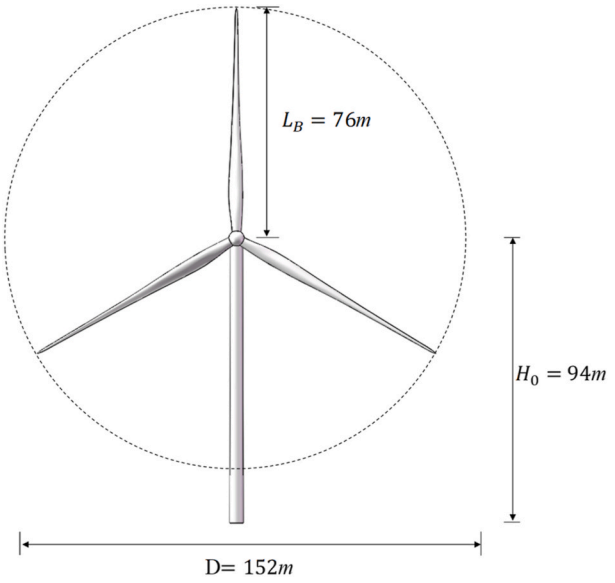

Fig. 3. The three-dimensional wind turbine model.

Porté-Agel, 2012; Ishihara and Qian, 2018; Sayed et al., 2019a). It was found that the wake boundary expansion and maximum velocity deficit at the hub height level can vary subsequently. The influence of atmospheric stability was investigated as well (Guo et al., 2021). Tian et al. (2018) compared the velocity deficit behind wind turbine obtained by RANS models with different inflow profiles and found that the difference is small and can be negligible. Regarding elastic blade models, studies have examined the velocity deficit in the wake region under uniform winds (Leng et al., 2023), turbulent winds (Li et al., 2015) and ABL (Xu et al., 2023), respectively. However, the impact of inflow wind conditions on the wake characteristics generated by flexible blades and tower remains unclear and requires further investigation.

Furthermore, the vortex present in the wake region is created through the interaction between the rotating flow and surrounding air. The wake characteristics are affected by the flow fields around the blades. Piquee et al. (2022) investigated the mean velocity and vorticity around rigid and flexible blades and found clear differences. Whale et al. (2000) experimentally and numerically studied the flow structure in the wake region. Miao et al. (2019) studied the vorticity and streamline on blades and the pattern of vortex shedding considering straight and swept blades. The vortex structure of the wake is related to the interaction between the wind and the blades, and the flow dynamics of the wake can be explained by the flow fields on the blades and the pattern of vortex shedding that occurs when a wind turbine is operating. Further research in this area can yield important insights into wind turbine wake behavior.

Despite the extensive research that has been conducted on wind turbine wake characteristics, a knowledge gap still exists regarding the effects of blade and tower flexibility on wake characteristics under both uniform and turbulent winds, especially for large wind turbines. Consequently, the aim of the paper is to study impacts of blade flexibility, tower flexibility, and inflow conditions on wake characteristics. The main motivations of this study are as follows.

- To propose a coupled CFD-CSD method for investigating wind turbine wake characteristics while considering blade and tower flexibility.
- To examine the effects of blade and tower flexibility on wind turbine wake characteristics, including mean wind speed, turbulent intensity, and vortex variation in the wake region under both uniform and turbulent inflow conditions.
- To investigate the effects of blade and tower flexibility on vortex shedding, which primarily affects the wake characteristics of wind turbines, on both the blade and tower.

The structure of this paper is organized as follows: the theories and numerical methods used in the study are presented in section 2, the results including the mean velocity, turbulent intensity, wake vortex in the wake region, and the streamline on the blade and tower are shown section 3, while section 4 provides the conclusion for this research.

2. Theories and numerical methods

Section 2.1 and Section 2.2 introduce the CFD simulations and the computational structure dynamics are introduced. The coupled CFD-CSD model and the case settings are presented in section 2.3 and in section 2.4, respectively.

2.1. CFD simulations

2.1.1. Governing equations

The governing equations for LES can be obtained by filtering the time-dependent Navier-Stokes equations in physical space. This process effectively filters out small-scale turbulent eddies with low energy, resulting in a modified equation:

$$\widetilde{\Phi}(x) = \frac{1}{\Omega}\int_{\Omega} \Phi(x)dx, x \in \Omega \tag{1}$$

where $\sim$ shows filtering, $\Phi(x)$ presents the fluid variable, Ω refers to the volume.

Filtering the incompressible Navier-Stokes equations yields a set of equations:

$$\frac{\partial \rho \widetilde{u}_i}{\partial x_i} = 0 \tag{2}$$

$$\frac{\partial \rho \widetilde{u}_i}{t} + \frac{\partial \rho \widetilde{u}_i \widetilde{u}_j}{x_j} = \frac{\partial}{\partial x_j}\left(\mu \frac{\partial \widetilde{u}_i}{\partial x_j}\right) - \frac{\partial \widetilde{p}}{\partial x_i} - \frac{\partial \tau_{ij}}{\partial x_j} \tag{3}$$

where $\widetilde{u}_i$ and p are the filtered velocity and pressure, while τ_{ij} is the subgrid-scale (SGS) Reynolds stress, which can be obtained using an SGS stress model. In this study, the Smagorinsky model is used as the viscosity subgrid-scale model and it is expressed as follows:

$$\tau_{ij} = -2\mu_t \widetilde{S}_{ij} + \frac{1}{3}\tau_{kk}\delta_{ij} \tag{4}$$

$$\widetilde{S}_{ij} = \frac{1}{2}\left(\frac{\partial \widetilde{u}_i}{\partial x_j} + \frac{\partial \widetilde{u}_j}{\partial x_i}\right) \tag{5}$$

where μ_t is the SGS turbulent viscosity coefficient, $\widetilde{S}_{ij}$ is the strain rate

Table 2
Basic parameters for the different types of airfoils.

No.	Section radius (m)	Relative thickness (%)	Twist angle (。)	Chord length (m)	Airfoil
1	0	100	9.50	2.90	Cylinder
2	0.5	100	9.50	2.90	Cylinder
3	1	100	9.50	2.90	Cylinder
4	9.22	60	10.91	4.22	TR25-2 d
5	16.67	40	8.57	4.64	DU00-W2-401
6	23.82	35	6.60	4.09	DU00-W2-350
7	39.62	30	1.60	2.43	DU97-W-300
8	59.84	25	−1.02	1.29	DU91W2-250
9	69.04	21	−2.04	0.94	NACA-63421
10	72	18.00	−2.50	0.80	NACA-63618

tensor of the resolved scales, and δ_{ij} is the tensor product. The SGS turbulent viscosity coefficient is calculated using the Smagorinsky-Lilly model:

$$\mu_t = \rho L_s^2 |\widetilde{S}| = \rho L_S \sqrt{2\widetilde{S}_{ij}\widetilde{S}_{ij}} \tag{6}$$

$$L_s = \min\left(\kappa d, C_s V^{1/3}\right) \tag{7}$$

where L_s represents the SGS mixing length, κ is the von Karman constant (0.42), d is the distance to the nearest wall, and C_s is the Smagorinsky constant (0.01).

2.1.2. Computational domain and boundary condition

The dimensions of the computational domain are presented in Fig. 2, and include a length of 1700 *m*, a width of 456 *m*, and a height of 398 *m*. The wind turbine is situated 500 *m* from the inlet and 1200 *m* from the outlet, while the wake refinement zone spans a length of 300 *m*. In the center of the computational domain is a dynamic cuboid with dimensions of 100 *m* (length), 240 *m* (width), and 188 *m* (height). The rotation domain has a diameter of 170 *m* and extends 5 *m* forward and backward, resulting in a thickness of 10 *m*. The tower height is 94 *m*, with the blades and hub located within the rotation domain, and the tower, nacelle, and rotation domain situated within the dynamic domain. The boundary conditions for the computational domain are defined by symmetric boundaries on the sides and top, while the bottom boundary is represented as a wall. Furthermore, a velocity inlet serves as the source of incoming airflow, while a pressure outlet acts as the outlet. To generate the velocity inlet boundary condition, a turbulent wind profile is created using numerical simulation and mapped to the velocity inlet boundary.

Fig. 3 displays the three-dimensional wind turbine model with a hub height of 94 *m* and a rotor diameter of 152 *m*. The blade consists of one cylinder section and seven airfoil sections, namely TR25-2 d, DU00-W2-401, DU00-W2-350, DU97-W-300, DU91W2-250, NACA-63421, NACA-63618. A linear interpolation method is employed for the transition between two adjacent airfoils. The basic parameters of airfoils are summarized in Table 2.

2.1.3. Inflow boundary condition

To create a turbulent inflow condition, a numerical wind tunnel is constructed and validated by the wind tunnel test conducted by Ishihara et al. (2004). The turbulent wind on a plane in the numerical wind tunnel is extracted and considered as the inflow boundary condition. The computational domain for the numerical wind tunnel is shown in Fig. 4, with the length of 1550 *m*, the height of 180 *m*, and the width of 150 *m*. The boundary conditions of the numerical wind tunnel are consistent with those mentioned above, except for the velocity inlet with a constant wind velocity of 10 m/s. The extraction plane is situated 350 *m* downstream of the spire.

2.1.4. Numerical grid and dynamic mesh

The present study explored the calculation efficiency of the structured and unstructured grids when implementing the dynamic mesh technique. It is noted that the structured grids have a low grid update rate, which results in a 20-fold increase in time compared to unstructured grids when the same displacement is generated. Therefore, a hybrid numerical grid scheme is adopted as shown in Fig. 5 with the tetrahedral grid in the rotation and dynamic regions, and the hexahedral grid in the outer flow region. The rotation and dynamic regions are characterized by cylinder and square shapes, respectively, and the flow information is transformed through the interface. The mesh refinement region behind wind turbine has been built to capture wake vortices. The total number of numerical girds is about 7.17 million. The grid size for every region and the grid growth rate are illustrated in Table 3. A boundary layer grid was set on these surfaces with a first layer thickness of 0.008 *m*, a growth rate of 1.15, and a total of 7 layers. The resulting Y+ values were found to be around 1 for most regions on blade and tower, which is consistent with previous research by O'Brien et al. (2018).

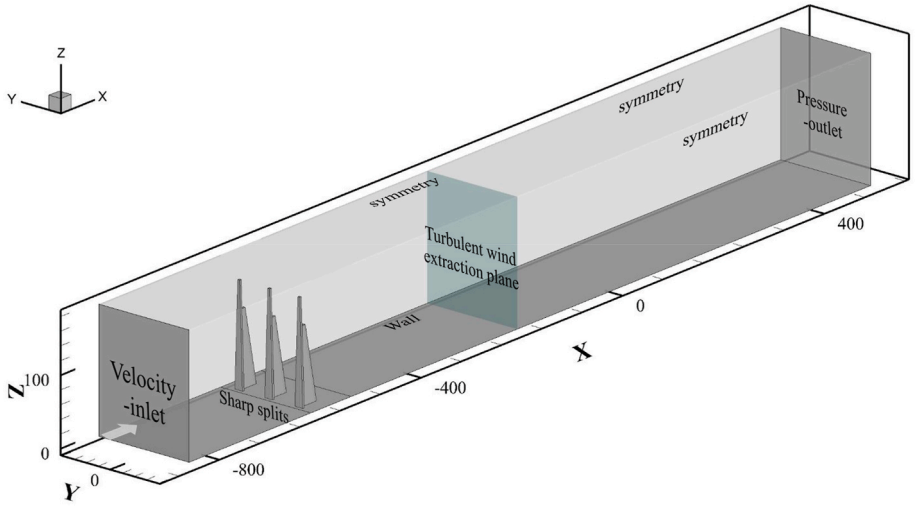

Fig. 4. Configurations of the numerical wind tunnel to generate the inflow winds.

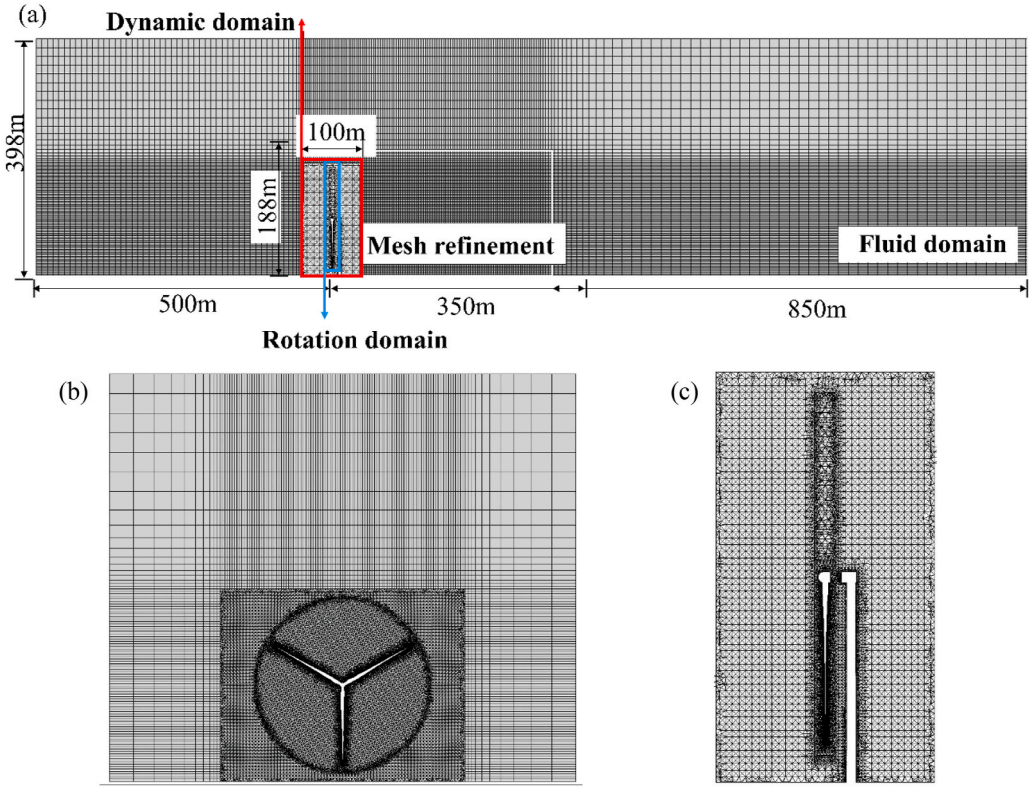

Fig. 5. Configuration of numerical grids with: (a) the fluid; (b) rotation; (c) dynamic domains.

Table 3
Numerical grid for different domains.

Region	Grid type	Minimum size (m)	Maximum size (m)	Space ratio	Grid quantity
Rotation	Tetrahedral	0.1	2.4	1.2	2.42 million
Dynamic	Tetrahedral	2.4	3.5	1.2	2.31 million
Outer flow	Hexahedral	2.4	17.0	1.1	2.45 million

The study incorporates both the sliding and dynamic mesh techniques for simulating the rotation and deformation of wind turbine blades and tower. The sliding mesh technique enables the modelling of rotating components while maintaining the non-rotating components grid. This technique is widely used in wind turbine and fan simulations. The dynamic mesh technique, on the other hand, allows for the computational domain grid to adapt to changes in the flow field during the CFD calculation process, improving the accuracy of simulations. The Fluent software package (Ansys Inc, 2022) provides various methods, including smoothing, dynamic layering, and local remeshing, for updating the volume grid in deforming regions. For this study, we have utilized the diffusion smooth method to balance numerical accuracy and cost efficiency.

Fig. 6 depicts the sliding mesh model used in this study. Data transfer between adjacent sliding planes primarily involves three steps: (1) identification of adjacent elements for each element; (2) interpolation at the centroid of the element; and (3) exchange of information between blocks associated with different processing. Regardless of the specific identification and interpolation methods used, the calculation of cell values is governed by the following equation:

$$\Phi(x) = \sum_{i=1}^{i=n} w_i \Phi_i(x) \tag{8}$$

where $\Phi(x)$ represents any fluid variable, w_i presents the weight of the ith adjacent element, and n is the number of adjacent elements.

In the context of the grid sliding process, it is essential to account for

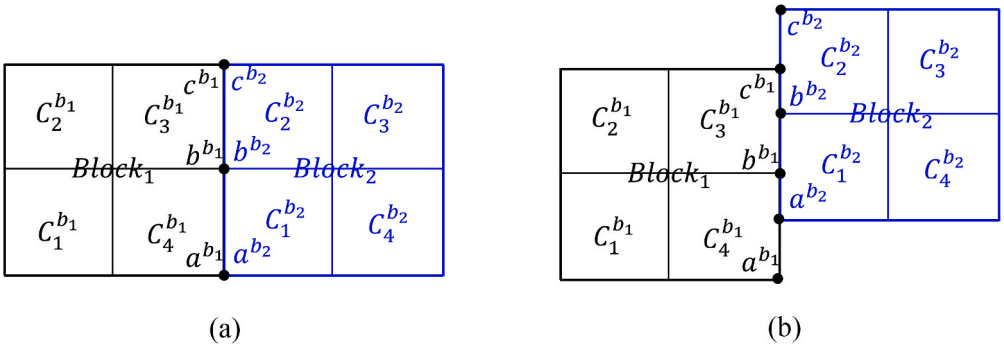

Fig. 6. The sliding grid with: (a) matching nodes; (b) unmatching nodes.

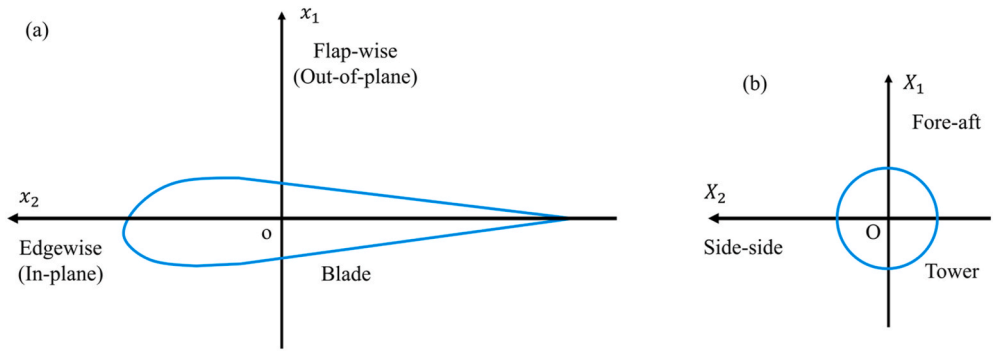

Fig. 7. Coordinate systems for: (a) the blade; (b) tower.

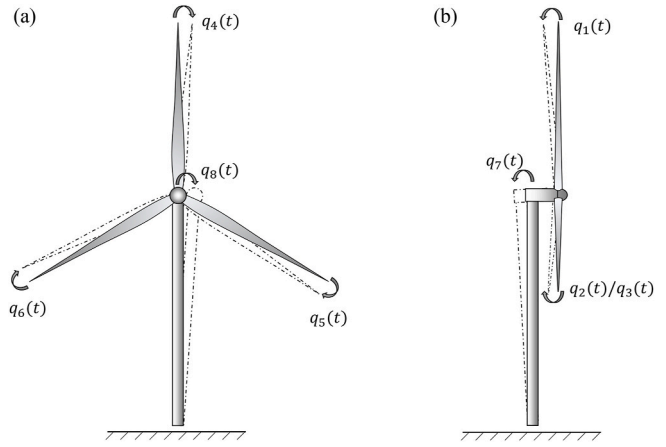

Fig. 8. Degrees of freedom for a wind turbine model.

the grid velocity of the moving block and adjust the N–S equation accordingly. The integral form of the governing equations for a moving volume element Ω bounded by a closed surface S is expressed as follows:

$$\oint_{\partial\Omega} \varphi(\mathbf{u}-\mathbf{u}_S)\cdot ndS = \oint_{\partial\Omega} \Gamma\nabla\varphi\cdot ndS + \int_{\Omega} q_\varphi d\Omega \tag{9}$$

The equation presented is capable of removing solely the velocity of the grid movement $\mathbf{u}_s$, whereas for the continuity constraint, the grid motion velocity should be satisfied:

$$\oint_{\partial\Omega} \mathbf{u}_S\cdot ndS = 0 \tag{10}$$

As the grid movement in this study occurs solely in the positive x-direction at a constant velocity, the aforementioned equation is inherently satisfied. Thus, while solving the N–S equation, the only modification required is to the fixed grid velocity in the momentum equation.

In the present study, the large displacements of the blade tip and tower top result in the possibility of negative mesh volume, which can increase the computational cost. To balance computational efficiency and model accuracy, the diffusion smoothing approach capable of accommodating large deformations is implemented. This approach is particularly effective in situations where the mesh is coarse, or the flow field undergoes significant changes. The diffusion smoothing algorithm is based on the discretized Laplacian operator and is applied to smooth the solution of the flow field, reducing the influence of grid size on the numerical solution. When calculating the flow rate between adjacent cells, a smoothing function is used to minimize fluctuations in the numerical solution. The algorithm computes the weighted average of the solution of each cell and the solution of adjacent cells using different weighting coefficients to control the degree of smoothing.

2.1.5. Solution methods

The unsteady three-dimensional governing equations are evaluated using ANSYS Fluent 2022 software (Ansys Inc, 2022), employing the finite volume method (FVM). The convective and viscous terms in the momentum equations are discretized using the second-order central difference scheme, while the unsteady terms are discretized using the second-order implicit scheme. In order to decouple the solution of pressure and velocities, the study employs the semi-implicit pressure linked equations (SIMPLE) algorithm. In this study, given a minimum grid size of 0.1 *m* in the rotating domain and an inflow wind speed of 10 m/s, the time step can be calculated using the Courant number value of 1. Therefore, the time step used in this study is set to be 0.01 *s*.

2.2. Computational structure dynamics

A structural dynamic model for wind turbines with 8 degrees of freedom is proposed by Liu et al. (2021c) where the modal shape is adopted to calculate the deflection of blade and tower. For each blade, a local coordinate system (x_1, x_2, x_3) is employed with its origin located at the root of the blade and x_1, x_2, and x_3 directions representing flap-wise, edgewise, and spanwise directions, respectively in Fig. 7(a). The tower and nacelle are represented by a global coordinate system (X_1, X_2, X_3) with its origin located at the tower base and the X_1, X_2, and X_3 directions corresponding to the windward, sideward, and upward directions, respectively in Fig. 7(b). Deflections of three blades along the x_1 and x_2 axes are denoted by $q_1(t) \sim q_3(t)$ and $q_4(t) \sim q_6(t)$ while the deflection of the tower along X_1 and X_2 axes is represented by $q_7(t)$ and $q_8(t)$ in Fig. 8.

Based on Euler-Lagrange stationary condition, the equations of motion for the wind turbine are derived and presented.

$$\mathbf{M}(t)\ddot{\mathbf{q}}(t) + \mathbf{C}\dot{\mathbf{q}}(t) + \mathbf{K}\mathbf{q}(t) = \boldsymbol{Q}(\dot{\mathbf{q}}(t), t) \tag{11}$$

where M(*t*), C, and K show the mass, damping and stiffness matrices, Q (q(t),t) is the external force.

The mass matrix $\mathbf{M}(t)$ mainly consists of two parts and can be expressed as follows:

$$\mathbf{M}(t) = \mathbf{M}_1(t) + \mathbf{M}_2 \tag{12}$$

where $\mathbf{M}_1(t)$ is supplied by blades, $\mathbf{M}_2$ is provided by the nacelle and tower. $\mathbf{M}_1(t)$ can be expressed as:

$$\mathbf{M}_1(t) = \begin{bmatrix} \mathbf{M}_{ll} & \mathbf{M}_{lg}(t) \\ \mathbf{M}_{gl}(t) & \mathbf{M}_{gg} \end{bmatrix} \tag{13}$$

$$\mathbf{M}_{ll} = \begin{bmatrix} m_{11} & 0 & 0 & 0 & 0 & 0 \\ 0 & m_{12} & 0 & 0 & 0 & 0 \\ 0 & 0 & m_{13} & 0 & 0 & 0 \\ 0 & 0 & 0 & m_{21} & 0 & 0 \\ 0 & 0 & 0 & 0 & m_{22} & 0 \\ 0 & 0 & 0 & 0 & 0 & m_{23} \end{bmatrix} \tag{14}$$

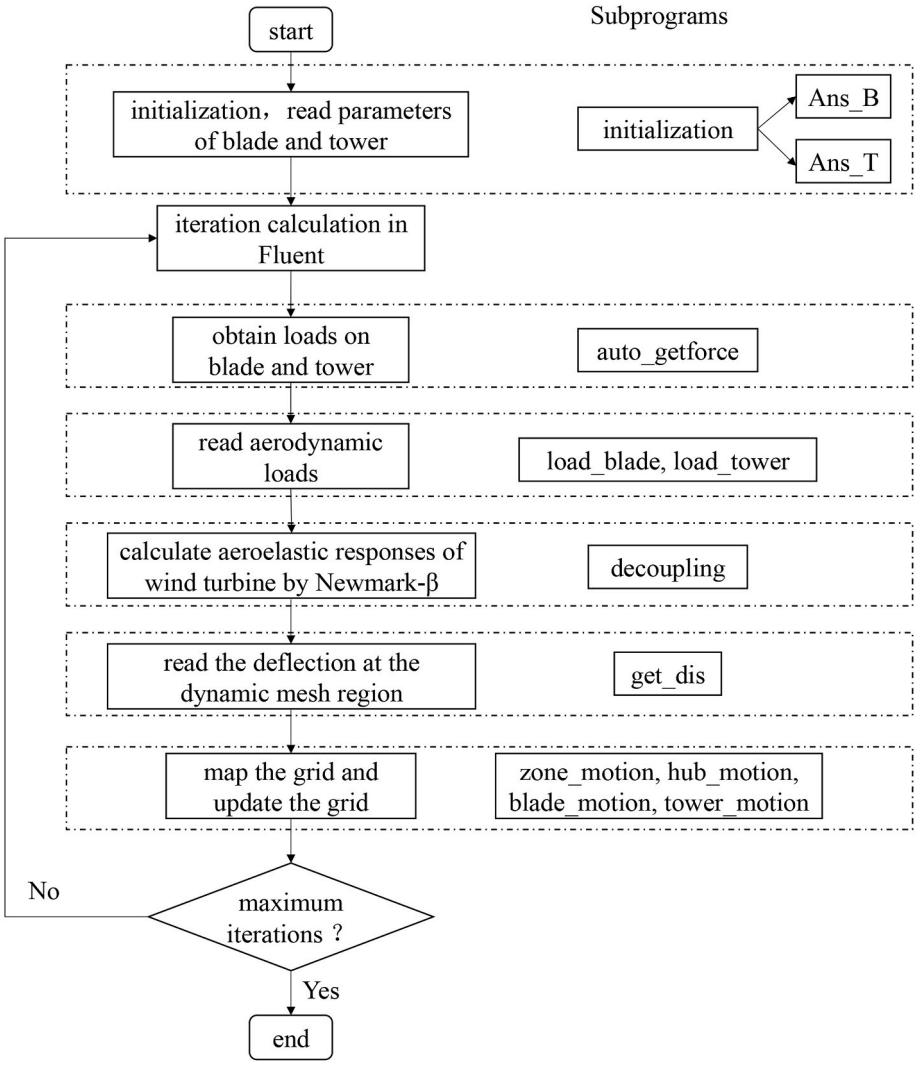

Fig. 9. The procedure of the coupled CFD-CSD model.

where m_{1j} and m_{2j} present the first-order generalized mass of the *jth* blade in the flap-wise and edgewise directions and can be calculated according to the following formulas.

$$m_{1j} = \int_0^R \mu_j(x_3)\left(\Phi_{1B}^j(x_3)\right)^2 dx_3 \tag{15}$$

$$m_{2j} = \int_0^R \mu_j(x_3)\left(\Phi_{2B}^j(x_3)\right)^2 dx_3 \tag{16}$$

where $\mu_j(x_3)$ stands for the mass per unit length for the *jth* blade, $\Phi_{1B}^j(x_3)$ and $\Phi_{2B}^j(x_3)$ display the first-order natural mode function of the *jth* blace in the flap-wise and edgewise directions.

$$\mathbf{M}_{gl}(t) = \begin{bmatrix} m_{11}^{l1} & m_{21}^{l1} & m_{31}^{l1} & m_{12}^{l1} & m_{22}^{l1} & m_{32}^{l1} \\ 0 & 0 & 0 & m_{12}^{l2} & m_{22}^{l2} & m_{32}^{l2} \end{bmatrix} \tag{17}$$

$$m_{j1}^{l1} = \int_0^{L_B} \mu_j(x_3)\left(\Phi_{1B}^j(x_3)\Phi_{1T}(\mathrm{H}_0) + x_3\cos\Psi_j(t)\right)dx_3 \tag{18}$$

$$m_{j2}^{l1} = \int_0^{L_B} \mu_j(x_3)\Phi_{2B}^j(x_3)\dot{\Phi}_{1T}(\mathrm{H}_0)s\cdot\sin\Psi_j(t)dx_3 \tag{19}$$

$$m_{j2}^{l2} = \int_0^{L_B} \mu_j(x_3)\Phi_{2B}^j(x_3)\dot{\Phi}_{2T}(\mathrm{H}_0)\cos\Psi_j(t)dx_3 \tag{20}$$

where $\Phi_{1T}(X_3)$ and $\Phi_{2T}(X_3)$ show the first-order natural mode function of the tower in the fore-aft and side-side directions.

$$\mathbf{M}_{gg} = \begin{bmatrix} m_{1g} & 0 \\ 0 & m_{2g} \end{bmatrix} \tag{21}$$

$$m_{1g} = \sum_{j=1}^{3}\left(\int_0^{L_B} \mu_j(x_3)\left(\left(\Phi_{1T}(\mathrm{H}_0) + \dot{\Phi}_{1T}(\mathrm{H}_0)x_3\cos\Psi_j(t)\right)^2 + \left(\dot{\Phi}_{1T}(\mathrm{H}_0)s\right)^2\right)dx_3\right) \tag{22}$$

$$m_{2g} = \sum_{j=1}^{3}\left(\int_0^{L_B} \mu_j(x_3)\left(\Phi_{2T}(\mathrm{H}_0)\right)^2 dx_3\right) \tag{23}$$

$\mathbf{M}_2$ provided by the nacelle and tower can be expressed as follows:

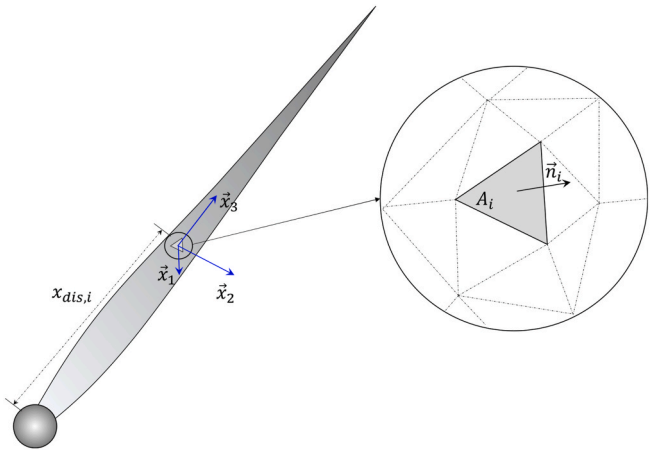

Fig. 10. Schematic diagram of aerodynamic load extraction grid.

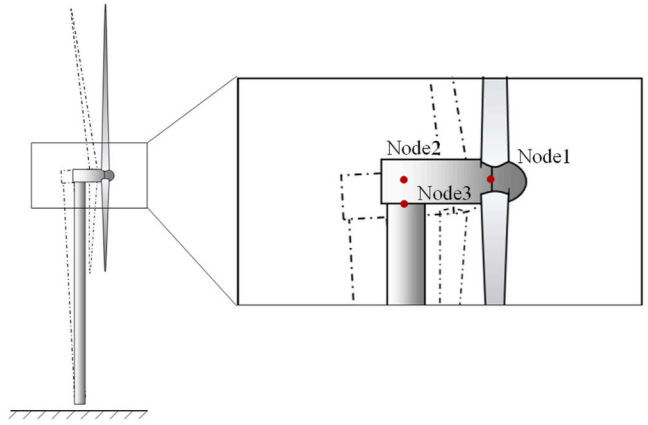

Fig. 11. The schematic diagram of controlling points for the grid mapping.

$$\mathbf{M}_2 = \begin{bmatrix} 0 & 0 & 0 & 0 & 0 & 0 & 0 & 0 \\ 0 & 0 & 0 & 0 & 0 & 0 & 0 & 0 \\ 0 & 0 & 0 & 0 & 0 & 0 & 0 & 0 \\ 0 & 0 & 0 & 0 & 0 & 0 & 0 & 0 \\ 0 & 0 & 0 & 0 & 0 & 0 & 0 & 0 \\ 0 & 0 & 0 & 0 & 0 & 0 & 0 & 0 \\ 0 & 0 & 0 & 0 & 0 & 0 & m_{1T} & 0 \\ 0 & 0 & 0 & 0 & 0 & 0 & 0 & m_{2T} \end{bmatrix} \tag{24}$$

$$m_{1T} = \int_0^{H_0} \mu_T(X_3)(\Phi_{1T}(X_3))^2 dX_3 + m_0(\Phi_{1T}(H_0))^2 \tag{25}$$

$$m_{2T} = \int_0^{H_0} \mu_T(X_3)(\Phi_{2T}(X_3))^2 dX_3 + m_0(\Phi_{2T}(H_0))^2 \tag{26}$$

where $\mu_T(X_3)$ represents the mass per unit length for the tower.

The stiffness matrix $\mathbf{K}$ also consists of two parts.

$$\mathbf{K} = \begin{bmatrix} \mathbf{K}_l & 0 \\ 0 & \mathbf{K}_g \end{bmatrix} \tag{27}$$

where $\mathbf{K}_l$ and $\mathbf{K}_g$ are the stiffness matrix supplied by the blades and tower, respectively.

$$\mathbf{K}_l = \begin{bmatrix} k_{11} & 0 & 0 & 0 & 0 & 0 \\ 0 & k_{12} & 0 & 0 & 0 & 0 \\ 0 & 0 & k_{13} & 0 & 0 & 0 \\ 0 & 0 & 0 & k_{21} & 0 & 0 \\ 0 & 0 & 0 & 0 & k_{22} & 0 \\ 0 & 0 & 0 & 0 & 0 & k_{23} \end{bmatrix} \tag{28}$$

$$\mathbf{K}_g = \begin{bmatrix} k_{1T} & 0 \\ 0 & k_{2T} \end{bmatrix} \tag{29}$$

where k_1^j, k_2^j display the first-order generalized stiffness of the jth blade in the flap-wise and edgewise directions, k_1^T, k_2^T show the first-order generalized stiffness of the tower in the fore-aft and side-side directions, and they can be calculated according to the following formulas.

$$k_{1j} = \int_0^{L_B} EI_1 \left(\frac{\partial^2 \Phi_{1B}^j(x_3)}{\partial x_3^2}\right)^2 dx_3 + \Omega^2 \int_0^{L_B} \left(\mu_j(x_3) x_3 \int_0^{x_3} \left(\frac{\partial \Phi_{1B}^j(x_3)}{\partial x_3}\right)^2 dx_3\right) dx_3 \tag{30}$$

$$k_{2j} = \int_0^{L_B} EI_2 \left(\frac{\partial^2 \Phi_{2B}^j(x_3)}{\partial x_3^2}\right)^2 dx_3 + \Omega^2 \int_0^{L_B} \left(\mu_j(x_3) x_3 \int_0^{x_3} \left(\frac{\partial \Phi_{2B}^j(x_3)}{\partial x_3}\right)^2 dx_3\right) dx_3 \tag{31}$$

$$k_{1T} = \int_0^{H_0} EI_{1T} \left(\frac{\partial^2 \Phi_{1T} X_3}{\partial {X_3}^2}\right)^2 dX_3 + m_0 g \int_0^{H_0} \left(\frac{\partial \Phi_{1T}(X_3)}{\partial X_3}\right)^2 dX_3 + \int_0^{H_0} \left(\mu_T(X_3) g \int_0^{X_3} \left(\frac{\partial \Phi_{1T}(X_3)}{\partial X_3}\right)^2 dX_3\right) dX_3 \tag{32}$$

Table 4
Case settings.

Case	Uniform inflow	Turbulent inflow	Tower motion	Flap-wise motions of blades	Edgewise motions of blades	Index
1	●	○	○	○	○	W0T0B0b0
2	●	○	○	○	●	W0T0B0b1
3	●	○	○	●	○	W0T0B1b0
4	●	○	○	●	●	W0T0B1b1
5	●	○	●	○	○	W0T1B0b0
6	●	○	●	○	●	W0T1B0b1
7	●	○	●	●	○	W0T1B1b0
8	●	○	●	●	●	W0T1B1b1
9	○	●	○	○	○	W1T0B0b0
10	○	●	○	○	●	W1T0B0b1
11	○	●	○	●	○	W1T0B1b0
12	○	●	○	●	●	W1T0B1b1
13	○	●	●	○	○	W1T1B0b0
14	○	●	●	○	●	W1T1B0b1
15	○	●	●	●	○	W1T1B1b0
16	○	●	●	●	●	W1T1B1b1

●: adopt this inflow condition or consider the corresponding DoFs.
○: do not adopt this inflow condition or neglect the corresponding DoFs.

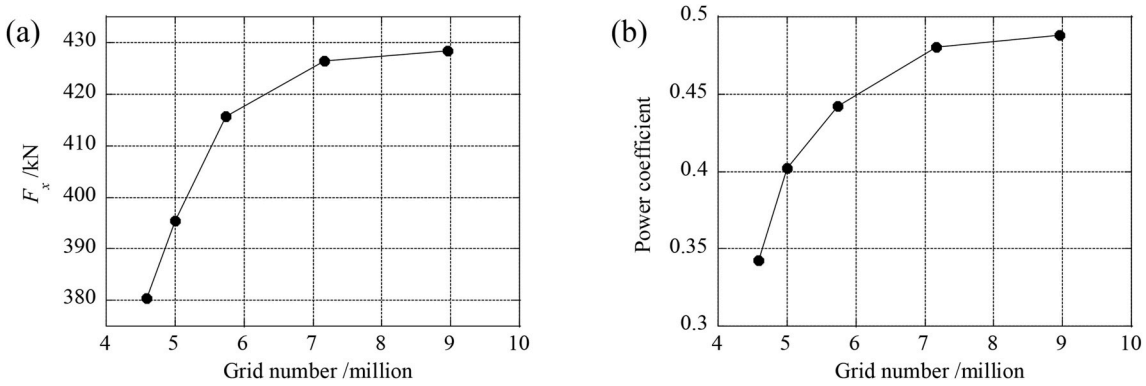

Fig. 12. Variations of the: (a) thrust force and; (b) power coefficient with the total number of numerical grids.

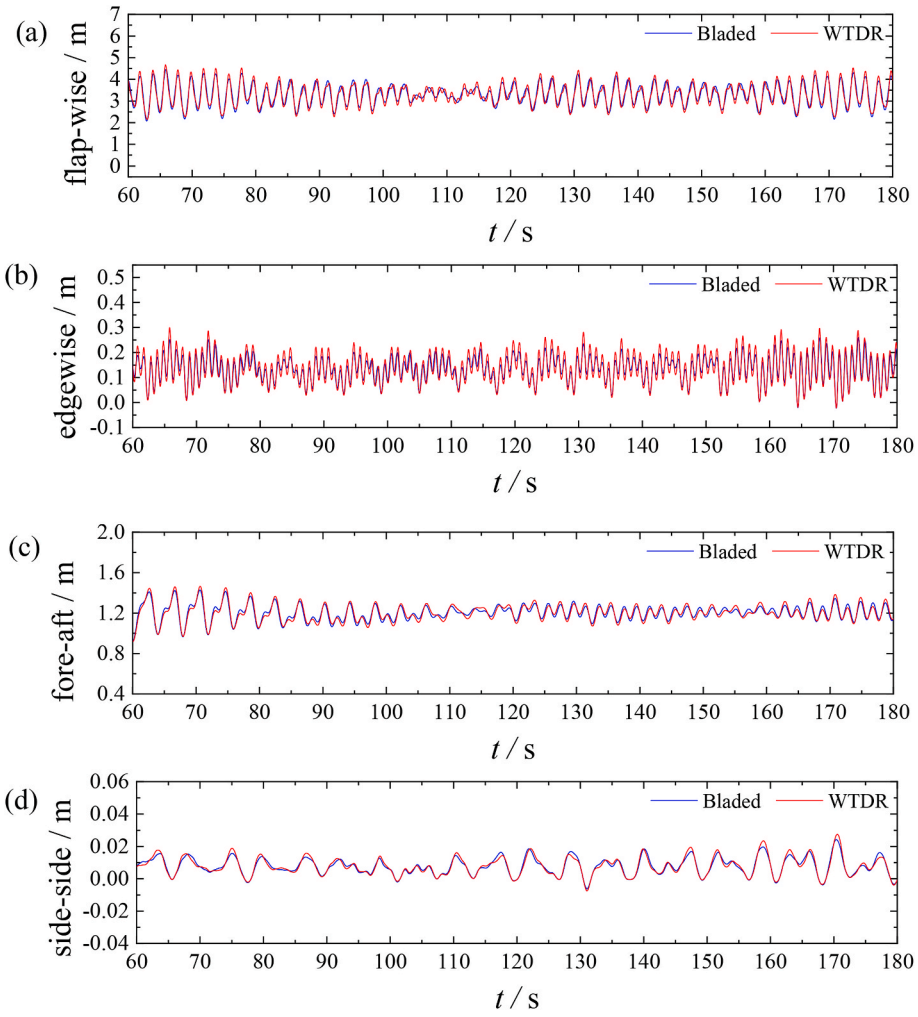

Fig. 13. Comparisons of displacements of wind turbines calculated by the coupled CFD-CSD model and the commercial software Bladed: (a) at the blade tip in the flap-wise direction; (b) at the blade tip in the edgewise direction; (c) at tower tip in the fore-aft direction; (d) at tower tip in the side-side direction.

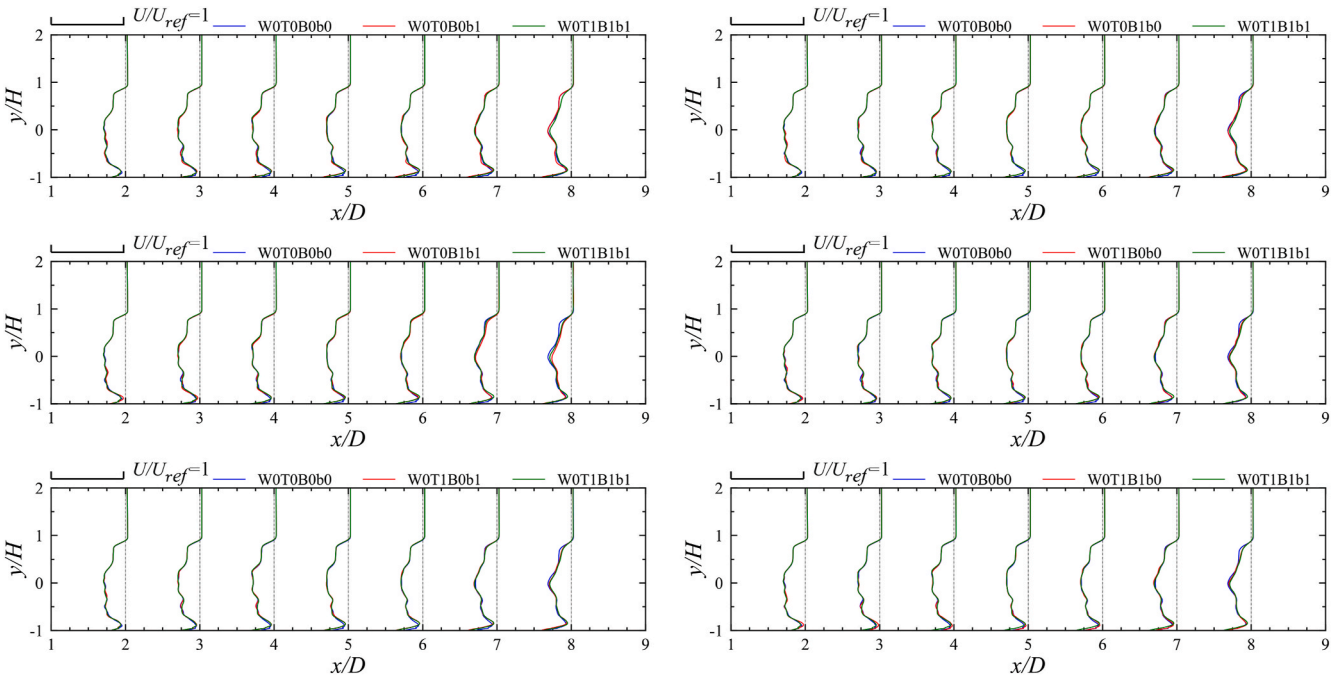

Fig. 14. Mean wind velocity within the vertical plane at the turbine center under uniform winds considering different blade and tower flexibilities.

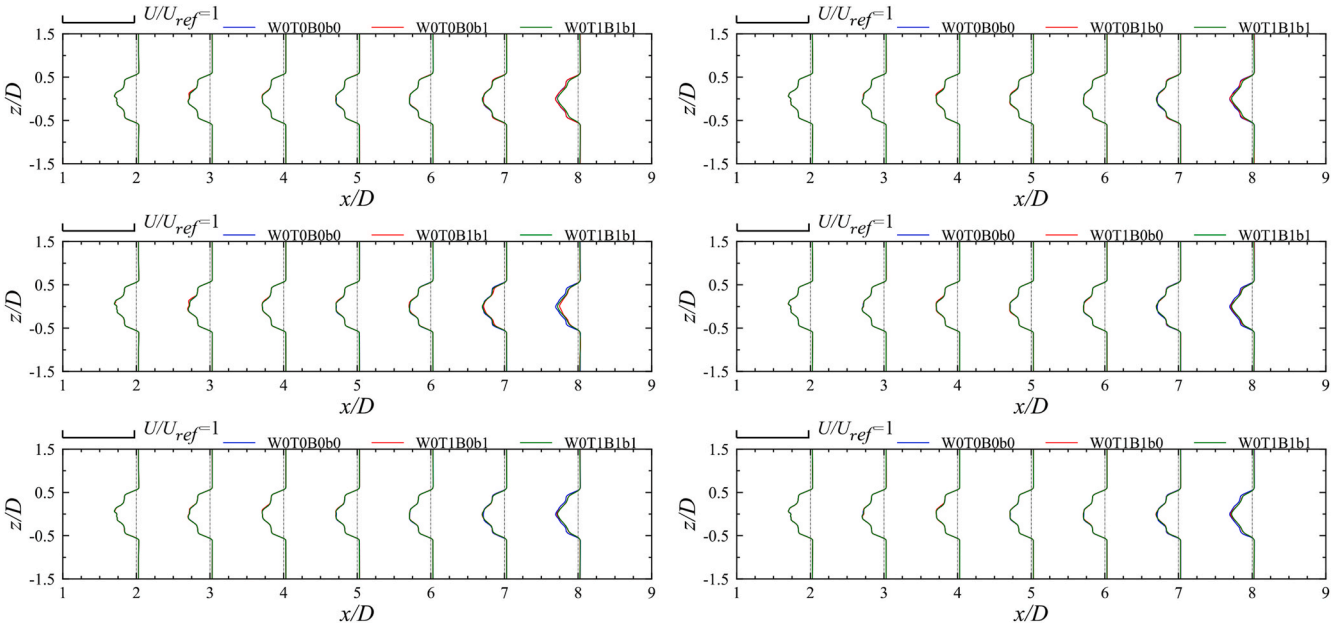

Fig. 15. Mean wind velocity within the lateral plane at the hub level under uniform winds considering different blade and tower flexibilities.

$$k_{2T}=\int_0^{H_0}\mathrm{EI}_{2T}\left(\frac{\partial^2\Phi_{2T}(X_3)}{\partial {X_3}^2}\right)^2 dX_3+m_0g\int_0^{H_0}\left(\frac{\partial\Phi_{2T}(X_3)}{\partial X_3}\right)^2 dX_3 + \int_0^{H_0}\left(\mu_T(X_3)g\int_0^{X_3}\left(\frac{\partial\Phi_{2T}(X_3)}{\partial(X_3)}\right)^2 dX_3\right)dX_3 \tag{33}$$

The damping matrix consisted of two parts and can be expressed as follows:

$$\mathbf{C}=\begin{bmatrix}\mathbf{C}_l & 0\\ 0 & \mathbf{C}_g\end{bmatrix} \tag{34}$$

where $\mathbf{C}_l$ and $\mathbf{C}_g$ are the structural damping of the blades and tower where the Rayleigh damping is adopted.

$$\mathbf{C}_l=\begin{bmatrix}c_{11}&0&0&0&0&0\\0&c_{12}&0&0&0&0\\0&0&c_{13}&0&0&0\\0&0&0&c_{21}&0&0\\0&0&0&0&c_{22}&0\\0&0&0&0&0&c_{23}\end{bmatrix} \tag{35}$$

$$\mathbf{C}_g=\begin{bmatrix}c_{1T}&0\\0&c_{2T}\end{bmatrix} \tag{36}$$

$$\left.\begin{aligned}c_{ij}&=2\xi_{ij}\sqrt{m_{ij}k_{ij}}\\ c_{iT}&=2\xi_{iT}\sqrt{m_{iT}k_{iT}}\end{aligned}\right\}\begin{matrix}j=1,2,3\\ i=1,2\end{matrix} \tag{37}$$

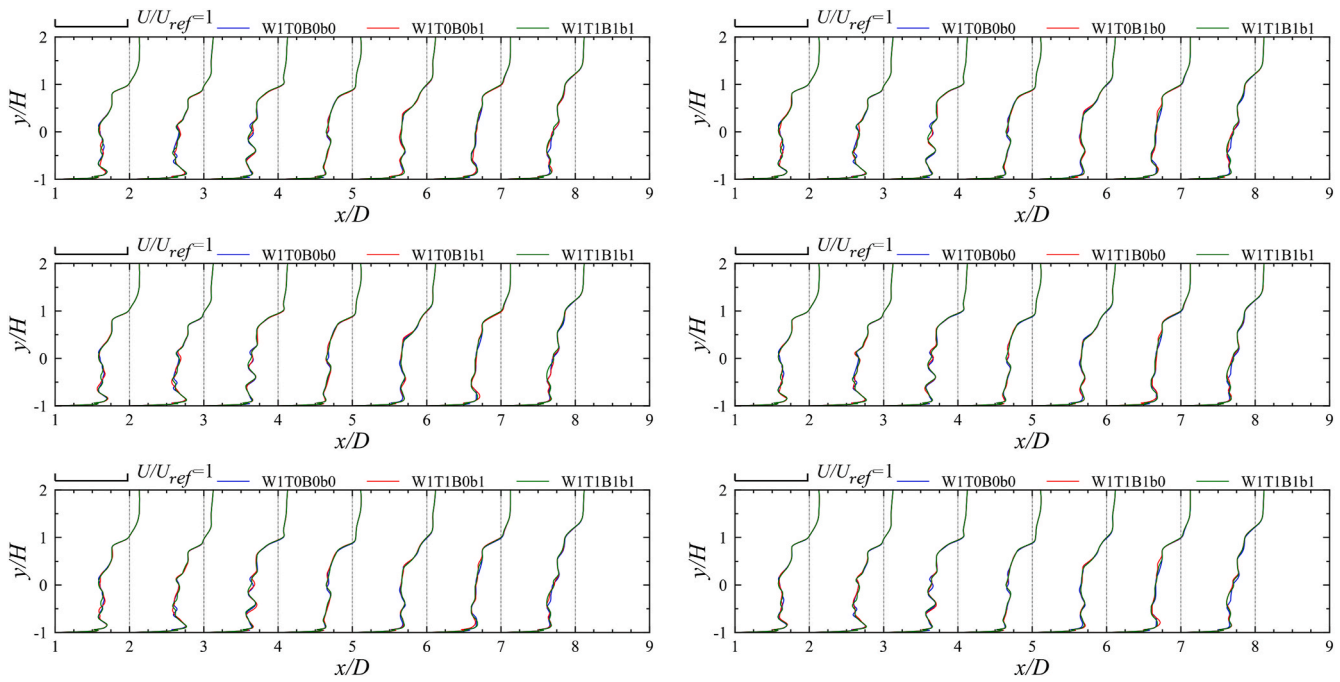

Fig. 16. Mean wind velocity within the vertical plane at the turbine center under turbulent winds considering different blade and tower flexibilities.

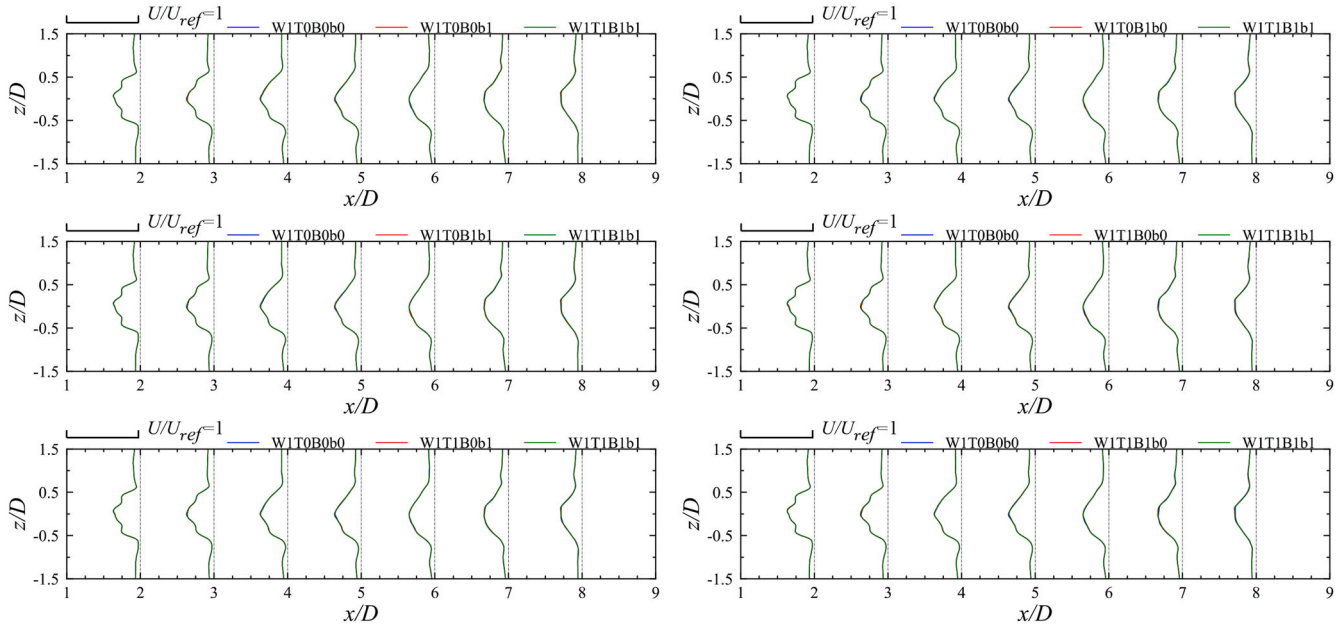

Fig. 17. Mean wind velocity within the lateral plane at the hub height under turbulent winds considering different blade and tower flexibilities.

where ξ_{ij}, ξ_{iT} show the damping ratio for the corresponding mode of blades and tower.

2.3. A coupled cfd-csd model

Fig. 9 illustrates the procedure of the coupled CFD-CSD model. Initially, the aerodynamic loads on the blade and tower are calculated by CFD simulations, followed by the structural response obtained using the CSD after inputting the aerodynamic loads into the structural dynamics model. Displacement is then read and mapped to the grid model, updating the grid. The iteration process continues until the maximum iteration is achieved. The subroutine controlling the grid deformation is divided into four parts: the displacement of the rotating domain, the displacement of hub, and the deformation of the blade and tower. Since the rotation domain produces the same displacement and inclination as the top of the tower deforms, the rotation center and axis need to be updated in real-time. The hub solely produces displacement, while the blades and tower deform and generate displacement during the calculation process, necessitating specification of motion for each grid node.

To successfully conduct the FSI analysis, accurate extraction of aerodynamic loads and numerical grid mapping are crucial. The study utilizes a coordinate projection method, as depicted in Fig. 10, to obtain the blade surface load. The aerodynamic loads, namely, the thrust force T, tangential force Q, and bending moment M, are determined using the following expressions:

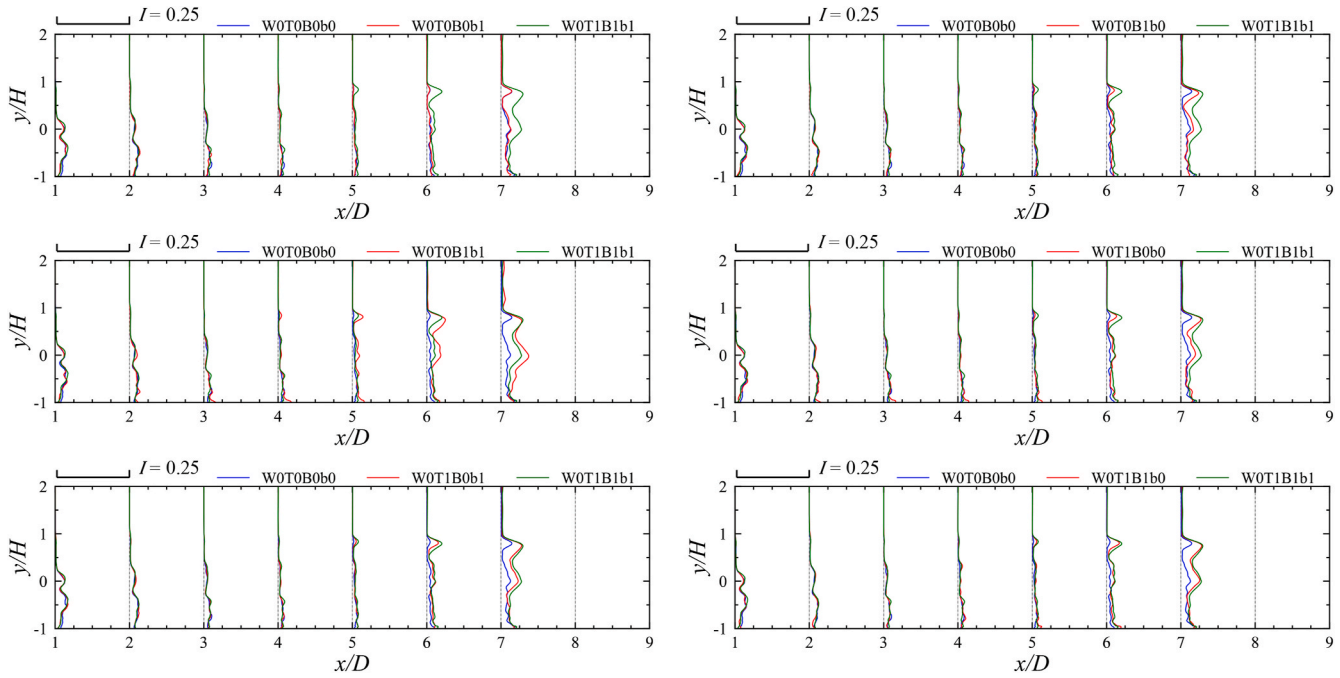

Fig. 18. Turbulent intensity within the vertical plane in the turbine center under uniform winds considering different blade and tower flexibilities.

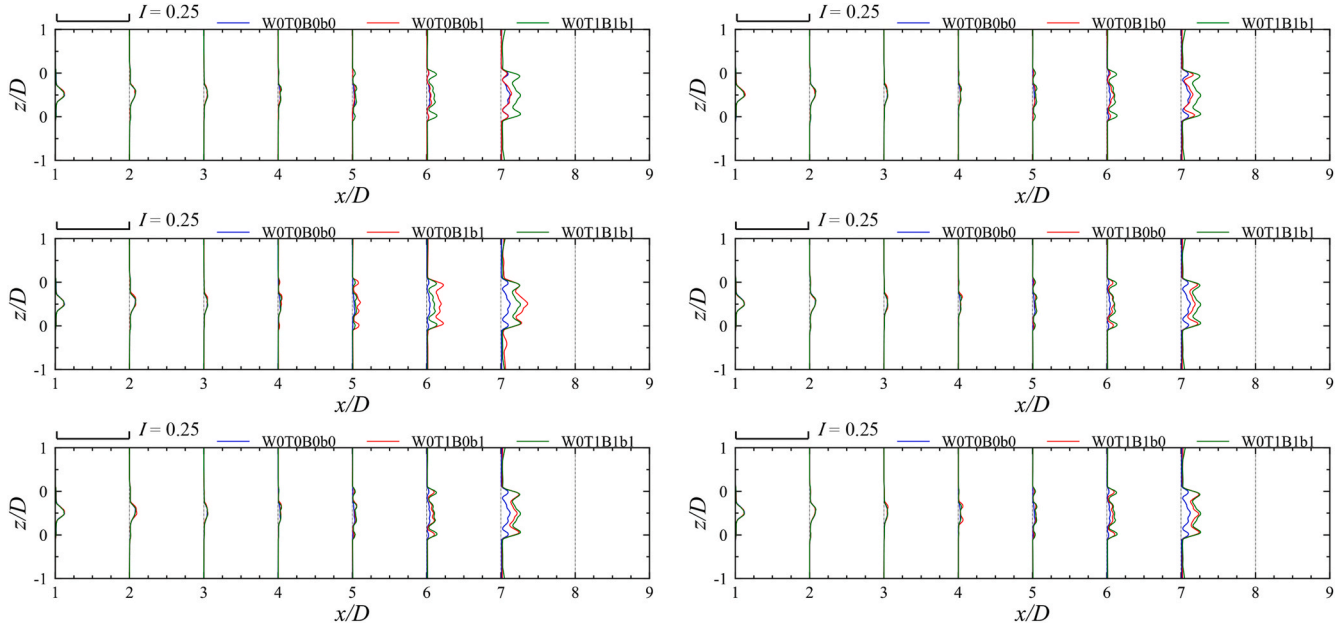

Fig. 19. Turbulent intensity within the lateral plane at the hub level under uniform winds considering different blade and tower flexibilities.

$$T = \sum_{i=1}^{n} A_i \cdot p_i \cdot \vec{n}_i \cdot \vec{x}_1 \tag{38}$$

$$Q = \sum_{i=1}^{n} A_i \cdot p_i \cdot \vec{n}_i \cdot \vec{x}_2 \tag{39}$$

$$M = \sum_{i=1}^{n} A_i \cdot p_i \cdot \vec{n}_i \cdot \vec{x}_2 \cdot x_{dis,i} \tag{40}$$

where $\vec{n}_i$ shows the area normal vector of the ith grid cell on the blade surface, p_i displays the surface pressure on the grid, A_i presents the area of the grid cell, $x_{dis,i}$ represents the distance between grid center and the center of nacelle, $(\vec{x}_1, \vec{x}_2, \vec{x}_3)$ are the local coordinate system that follows the blade rotation.

In this study, the employing the axis-angle method is utilized to calculate the three-dimensional coordinates of the rotated grid nodes. To obtain a new vector v', the vector v in three-dimensional space is rotated around a unit vector u with an angle of θ, as per the following formula. The calculation of the rotated coordinate of any node requires the knowledge of the basic information, such as the node coordinate, the rotation center coordinate, the rotation direction, and the rotation angle. The axis-angle method is the preferred method for the numerical simulation of fluid-structure interaction, which enables efficient calculation of the motion of the grid points.

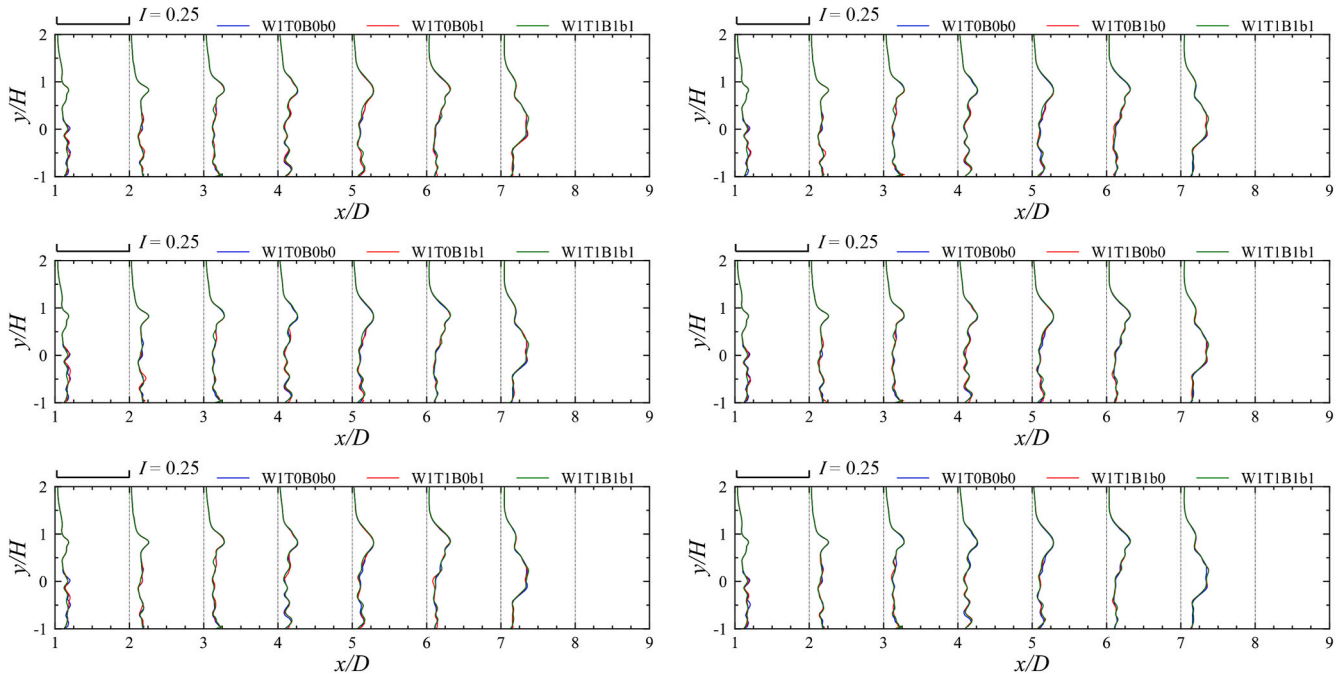

Fig. 20. Turbulent intensity within the vertical plane in the turbine center under turbulent winds considering different blade and tower flexibilities.

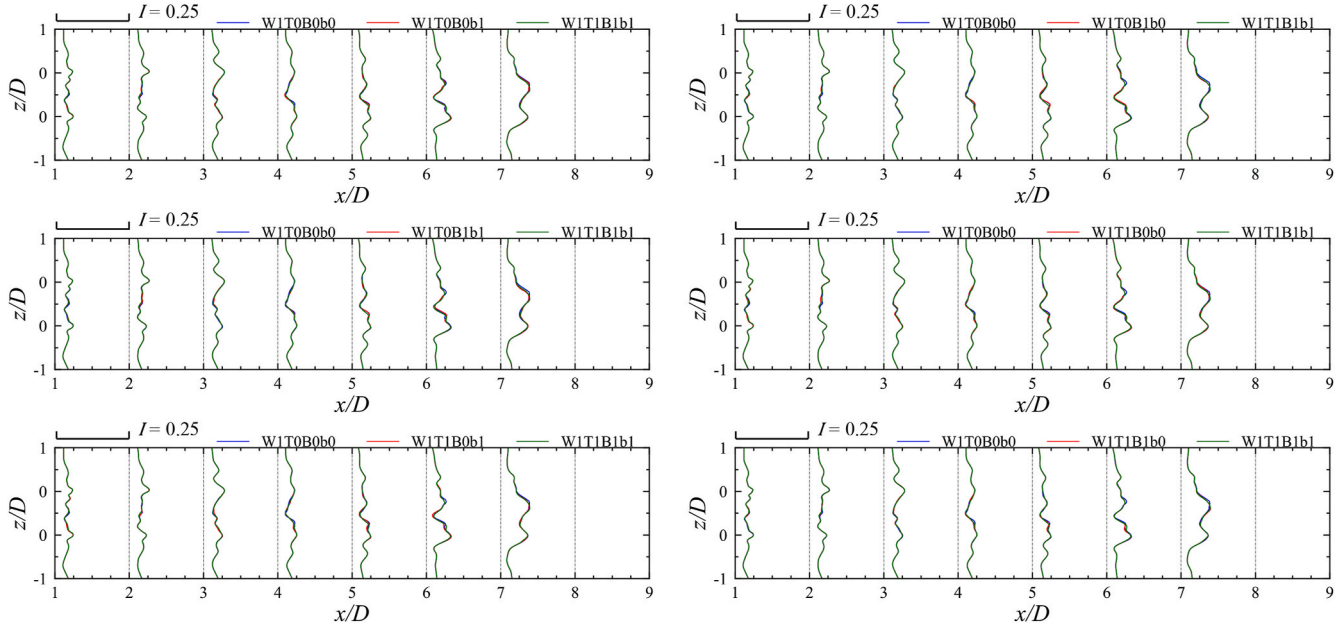

Fig. 21. Turbulent intensity in the lateral plane at the hub level under turbulent winds considering different blade and tower flexibilities.

$$\mathbf{v}' = \cos(\theta)\mathbf{v} + (1 - \cos(\theta))(\mathbf{u} \cdot \mathbf{v})\mathbf{u} + \sin(\theta)(\mathbf{u} \times \mathbf{v}) \tag{41}$$

As depicted in Fig. 11, a 3D model with three control nodes is employed. The three control nodes are referred to as the rotor rotation center (Node1), the nacelle center (Node2), and the nacelle rotation center (Node3). Initially, Node1 and Node2 are positioned on the same horizontal line, while Node2 and Node3 are located on the same vertical line. During the computation process, these control nodes move along with the deflection of the nacelle and hub. Real-time calculations are carried out based on the coordinates of these three control nodes to determine the flap-wise direction vector $\boldsymbol{u}_b$ and the edgewise direction vector $\boldsymbol{v}_b$ of the blade. However, these calculations do not consider the rotation motion.

$$\boldsymbol{u}_{\mathrm{b}} = \mathbf{X}_{\mathrm{Node2}} - \mathbf{X}_{\mathrm{Node1}} \tag{42}$$

$$\boldsymbol{n}_{\mathrm{b}} = \mathbf{X}_{\mathrm{Node3}} - \mathbf{X}_{\mathrm{Node2}} \tag{43}$$

$$\boldsymbol{v}_b = \boldsymbol{u}_b \times \boldsymbol{n}_b \tag{44}$$

The direction vector of the ith blade in the edgewise direction $\boldsymbol{v}_{b,i}$ can be obtained by rotating the direction vector $\boldsymbol{v}_b$ along the rotating vector $\boldsymbol{u}_b$ with the angle of θ.

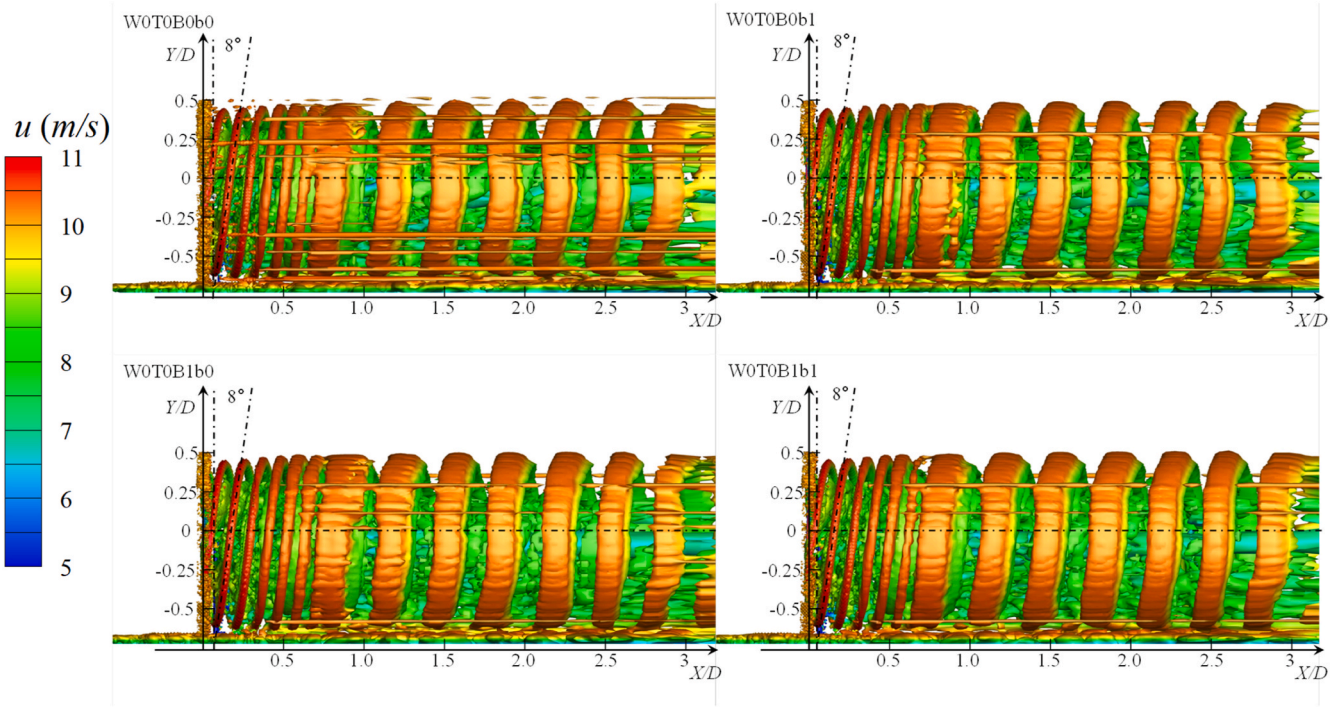

Fig. 22. Iso-surfaces of Q values colored by the instantaneous streamwise velocity for cases with a rigid tower under uniform inflow condition.

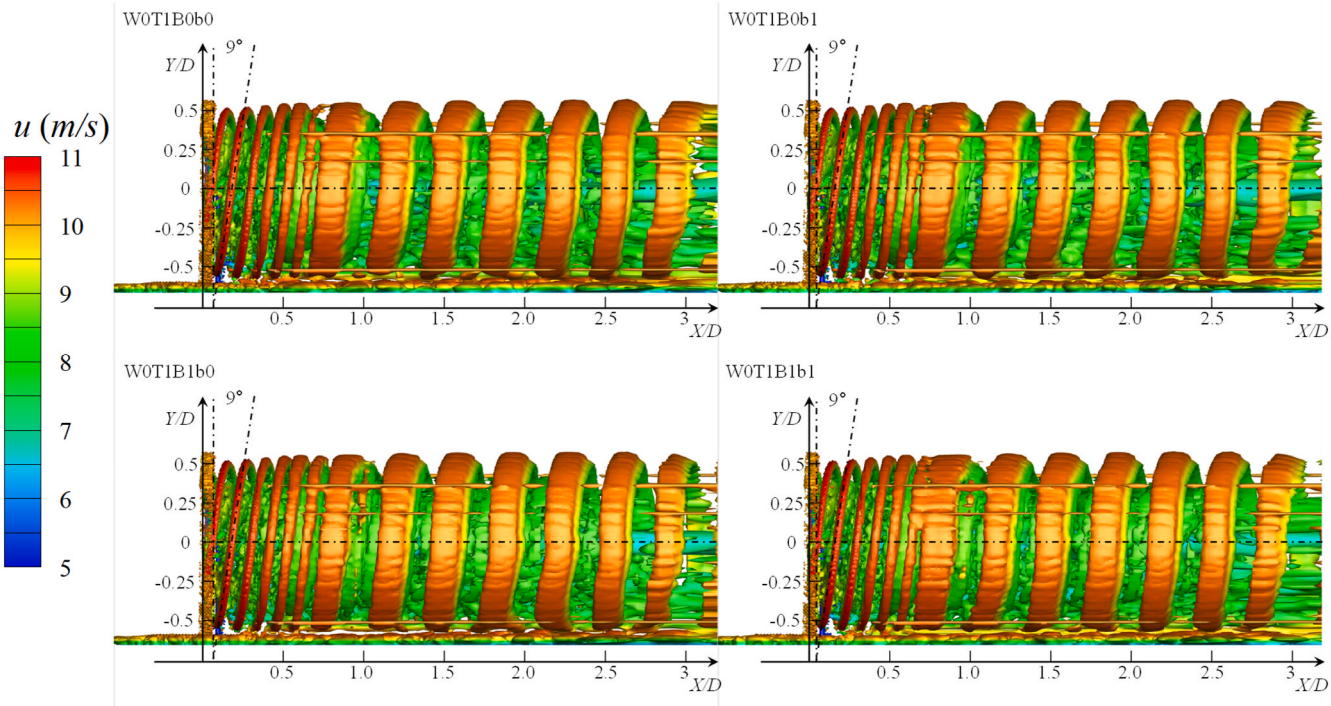

Fig. 23. Iso-surfaces of Q values colored by the instantaneous streamwise velocity for cases with a flexible tower under uniform inflow condition.

Table 5
Summary of the inclination angles under different cases.

	Rigid tower	Flexible tower
Uniform	8°	9°
Turbulent	10°	11°

$$\theta = \frac{2}{3}\pi(i-1) + \Omega t \quad i = 1, 2, 3 \tag{45}$$

where Ω shows the rotational speed, t is time.

The new position of grid node at each position of the blade in the global coordinate system can be updated as follows:

$$\mathbf{X}_{i,\text{new}} = \mathbf{X}_{i,\text{old}} + \mathbf{X}_{i,\text{old}} \cdot \frac{q_i(t)}{\|v_{b,i}\|} \cdot \Phi_{1B}(x_3) + \mathbf{X}_{i,\text{old}} \cdot \frac{q_{i+3}(t)}{\|v_{b,i}\|} \cdot \Phi_{2B}(x_3) + \mathbf{q}(t) \tag{46}$$

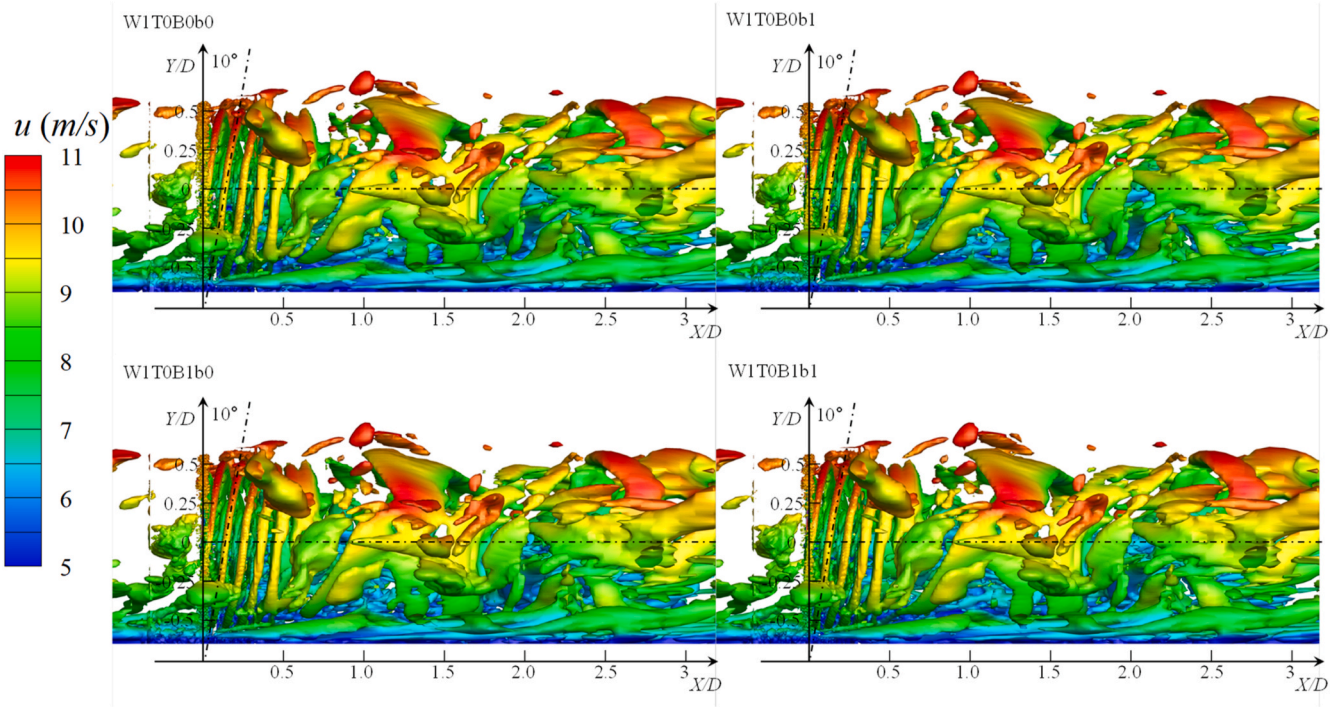

Fig. 24. Iso-surfaces of Q values colored by the instantaneous streamwise velocity for cases with a rigid tower under turbulent inflow condition.

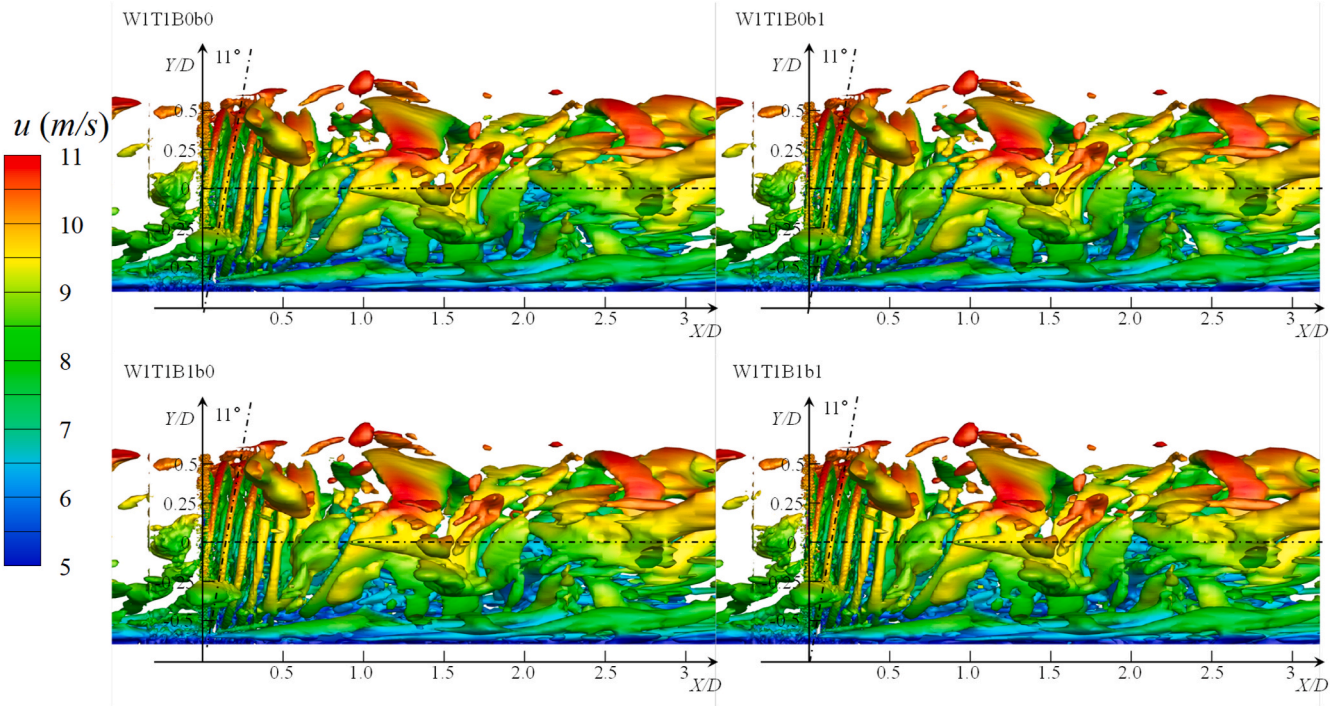

Fig. 25. Iso-surfaces of Q values colored by the instantaneous streamwise velocity for cases with a flexible tower under turbulent inflow condition.

2.4. Case settings

This study investigates the wind turbine wake characteristics in both uniform and turbulent winds through a FSI model. To enhance computational efficiency, the influence of different blade and tower flexibility on aerodynamic loads and aeroelastic responses is also explored. A total of 16 cases are considered, with the first eight cases subjected to uniform inflow and the latter eight exposed to turbulent inflow. The DoFs of the blades and tower in the different directions are either considered or neglected in different cases, as summarized in Table 4. Specific case names are listed in the final column, with the "W" indicating the inflow condition, "T" representing the tower's DoFs, and "B" and "b" indicating the DoFs of blades in the flap-wise and edgewise directions, respectively. The numbers "1" and "0" encode whether the specific degree of freedom is either included or removed, respectively. For instance, W0T0B0b0 indicates uniform inflow condition with all DoFs are removed, thus

adopting the one-way FSI simulation. In contrast, W1T1B1b1 refers to the two-way FSI simulation under turbulent inflow condition, as all eight DoFs are considered. A specific degree of freedom can be omitted by increasing the corresponding stiffness of the material.

The simulation times for cases under uniform and turbulent wind conditions are fixed at 200 s and 250 s respectively. For cases conducted under turbulent winds, the wind turbine does not undergo rotation during the initial 50 s to save the computational resources.

3. Results and discussion

The grid independency analysis and verification of the coupled CFD-CSD model are carried out in section 3.1. The averaged wind velocity and the turbulent intensity in the wake region are presented in section 3.2 and in section 3.3, respectively. The visualization of wake and the streamlines on the blade and tower are investigated in section 3.4 and in section 3.5, respectively.

3.1. Grid independency analysis and verification the coupled CFD-CSD model

The grid independency analysis is conducted by incrementally decreasing the chordal and spanwise grid sizes of the blade, resulting in five grid cases with the grid quantities of 4.59 million, 5.00 million, 5.74 million, 7.17 million, and 9.00 million. A full rotation of the blade at 10 rpm and an inflow wind speed of 10 m/s is used to calculate the axial thrust on the tower base. It is observed in Fig. 12 that the variation in thrust force and power coefficient tend to stabilize once the total number of grids exceeds 7 million. The relative error of the last two grid cases is found to be 0.42% for thrust force, satisfying the criteria for grid independence. Therefore, for a balance between computational cost and accuracy, the study selected the fourth grid case with 7.17 million numerical grids.

The accuracy of the coupled CFD-CSD model is verified by the commercial software GH Bladed (Bossanyi, 2003), as illustrated in Fig. 13. As shown in Table 1, the BEM theory is used in the commercial

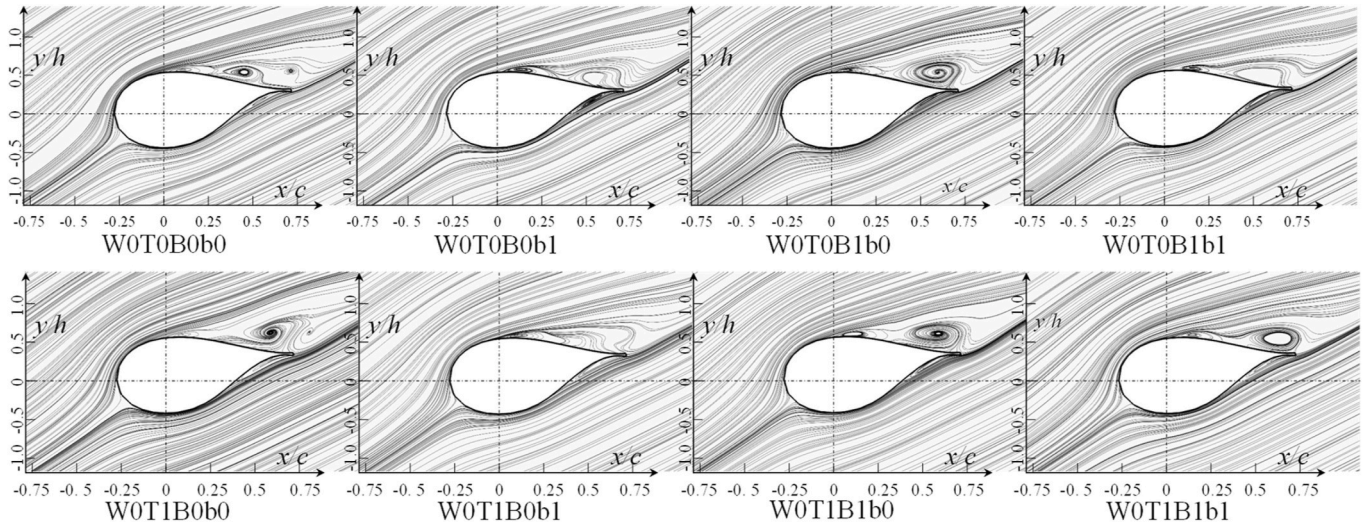

(a) at the 1/5 position

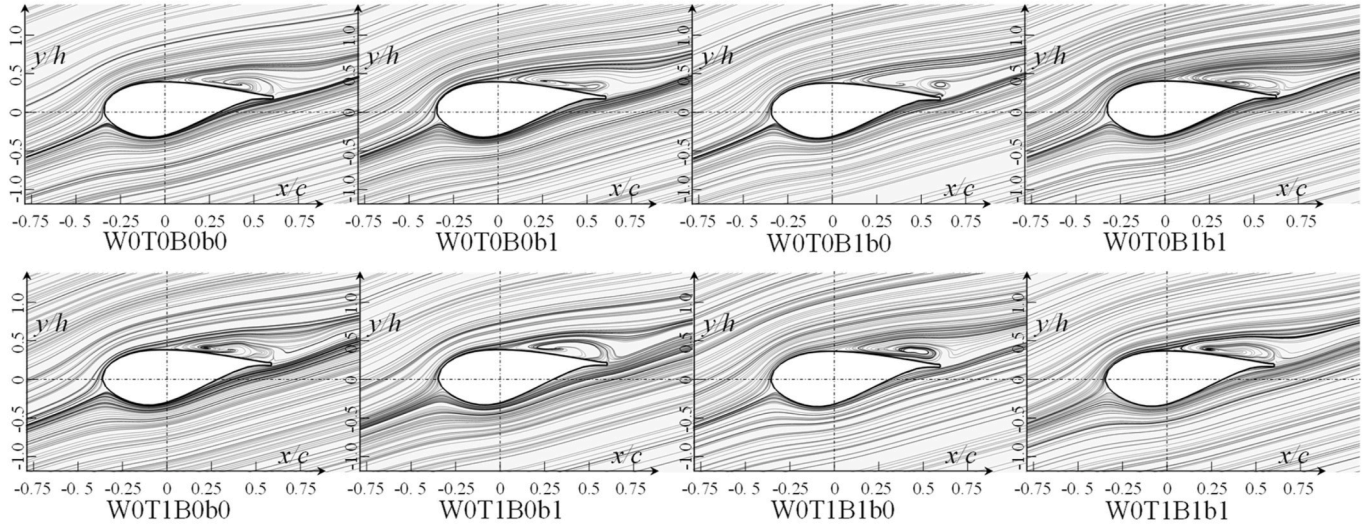

(b) at the 2/5 position

Fig. 26. Cross-sectional streamline on the blade root under uniform inflow condition considering blade and tower flexibility.

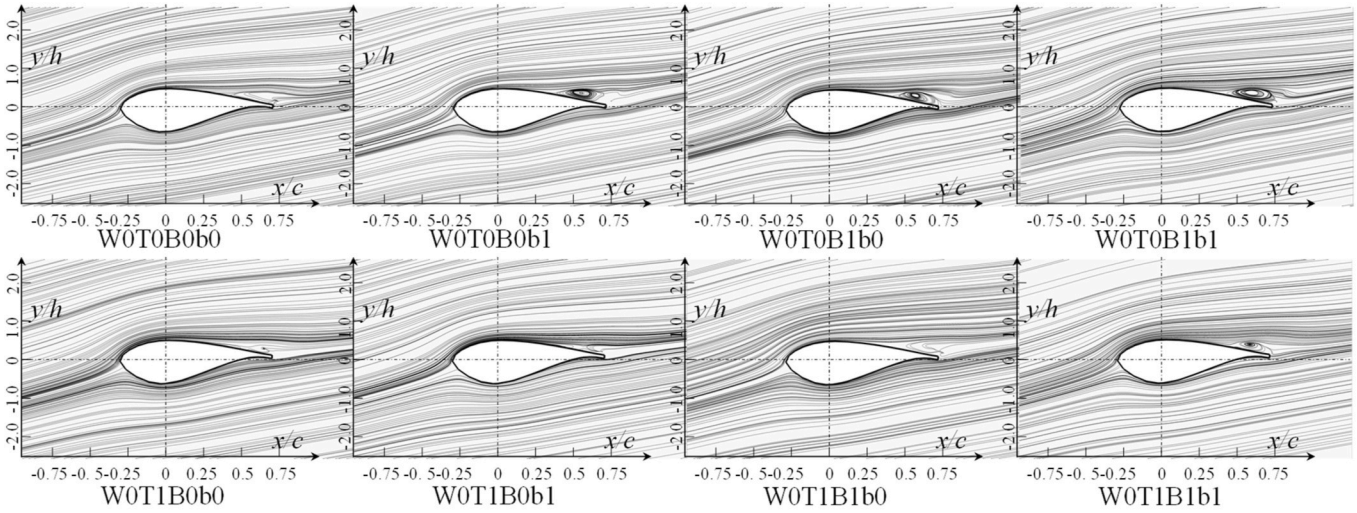

(c) at the 3/5 position

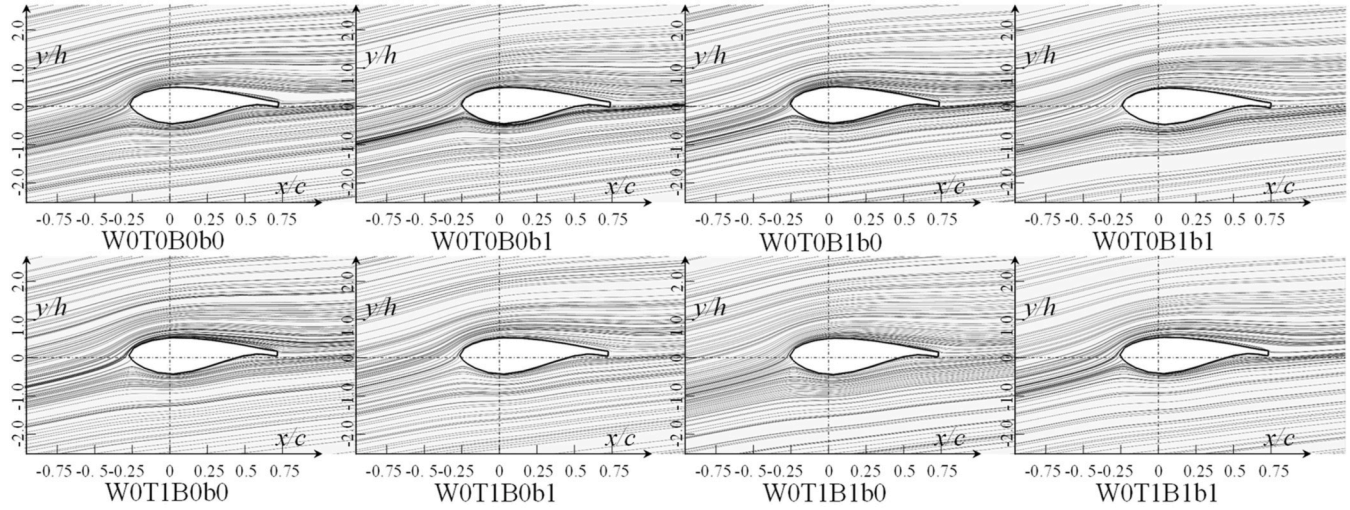

(d) at the 4/5 position

Fig. 26. (*continued*).

software GH Bladed to calculate the aerodynamic loads. The turbulent inflow condition used in this study is similar to that used in a previous study by Liu et al. (2021c), and the vertical profiles of mean wind speed and turbulence intensity are validated using experiments. Subsequently, the mean wind speed and turbulence intensity at the hub height are used as the wind conditions entering the commercial software GH Bladed. After obtaining the aerodynamic loads, the displacements at the blade tip and tower top are calculated using both methods. The GH Bladed considers the blade and tower as rigid bodies, whereas the proposed model constrains all degrees of freedom inherent to both blade and tower, effectively rendering these components rigid. It is observed that the flap-wise and edgewise displacements at the blade tip have a higher frequency of vibration than the tower top displacement. Additionally, it is important to note that the calculations conducted by both methods are one-way FSI analysis, which means that all wind turbine components are rigid during the CFD simulation. The results obtained from both methods are similar, demonstrating the accuracy of coupled CFD-CSD model in evaluating the structural responses of wind turbines.

3.2. Mean wind velocity in the wake region

As illustrated in Fig. 14 through Fig. 17, the profiles of mean wind velocity in both the horizontal and vertical plane are examined in the wake region under both uniform and turbulent inflow conditions. An apparent velocity deficit can be observed in this region. The wind profile close to the rotor is serrated, which suggests that the effects of rotor are not uniform across different spatial positions behind it.

Under uniform winds, the flow lacks lateral kinetic energy due to low ambient turbulence intensity. This results in slow wake diffusion, leaving a significant velocity deficit even at x = 7D (see Figs. 14 and 15). In turbulent winds, however, the lateral and vertical kinetic energy of the inflow wind causes the flow mixing to accelerate, resulting in outward expansion of the wake. With increasing distance, the diffusion effect becomes more significant, and the velocity deficit decreases accordingly (see Figs. 16 and 17).

Considering different blade and tower flexibilities, little variation in mean wind velocity profiles at x = 7D under uniform flow conditions is observed. The fully rigid case (W0T0B0b0) exhibits a greater velocity deficit than the fully flexible case (W0T1B1b1), with blade flap-wise

motion having the greatest impact on the mean wind speed, followed by the tower motion, and blade edgewise motion having the smallest impact. However, this effect is negligible under turbulent wind conditions. This is likely due to a smaller blade amplitude under uniform flow, resulting in a bending state that reduces the efficiency of extracting energy at the blade tip. The bending state also causes a smaller velocity deficit than that of the fully rigid configuration. Although the blade is vibrating under turbulent wind conditions, the effect of this vibration is small on the wake field after time averaging. At the same time, the energy exchange between flows is more intense under turbulent winds, leading to almost identical mean wind speed profiles in the downstream positions.

3.3. Turbulence intensity

Turbulence intensity is commonly utilized to assess turbulence energy magnitude relative to the average flow energy. The present study investigates the profiles of turbulent intensity in the wake region under both uniform and turbulent inflow conditions. Specifically, Fig. 18 through Fig. 21 illustrate the vertical and horizontal plane profiles of turbulent intensity.

The wake region exhibits relatively low turbulence intensity behind the rotor, with velocity fluctuation amplitude and turbulence intensity gradually increasing with the downstream distance. While the near wake region experiences considerable velocity deficit, the lateral energy exchange is not severe. As the wake develops in the downstream distance, lateral energy exchange intensifies, significantly increasing velocity fluctuation amplitude and turbulence intensity across various spatial locations, particularly at the blade tip.

The current study examines the differences of turbulent intensity distribution considering blade and tower flexibility under uniform inflow conditions, which become increasingly prominent with wake development. Notably, fully rigid condition (W0T0B0b0) demonstrates the lowest turbulence intensity, with turbulence intensity steadily increasing as more degrees of freedom are open. Tower motion has the most significant impact on turbulence intensity, with a maximal increase in turbulence intensity at the blade tip (45% increase for rigid blades at x = 7D). Blade flap-wise motion has the second-largest impact, increasing the maximum turbulence intensity by approximately 33% (when neglecting other degrees of freedom), while blade edgewise

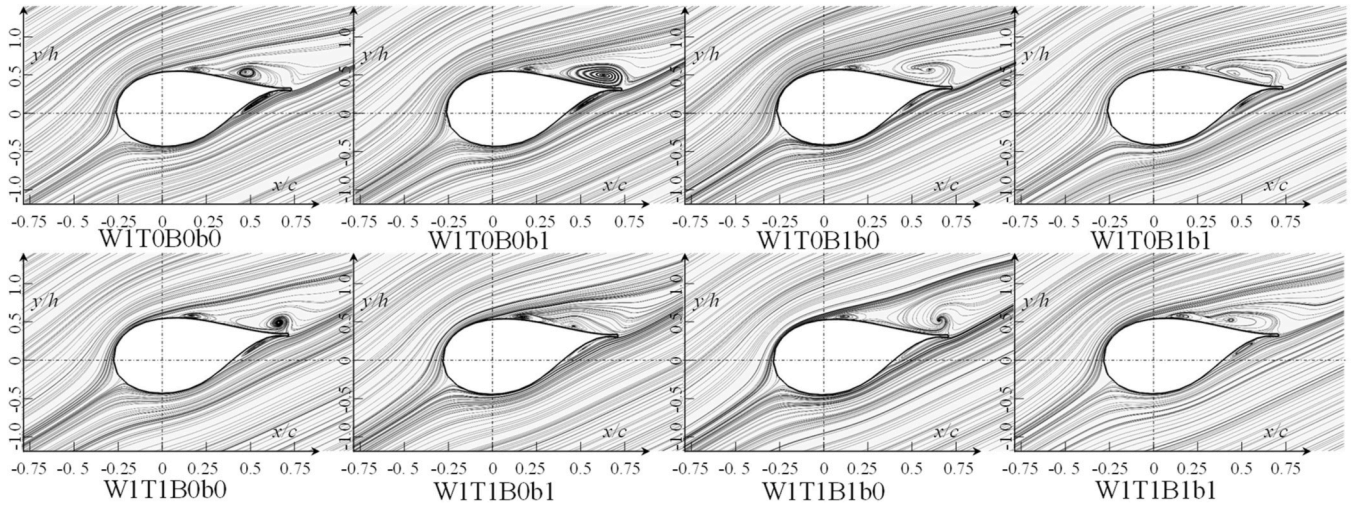

(a) at the 1/5 position

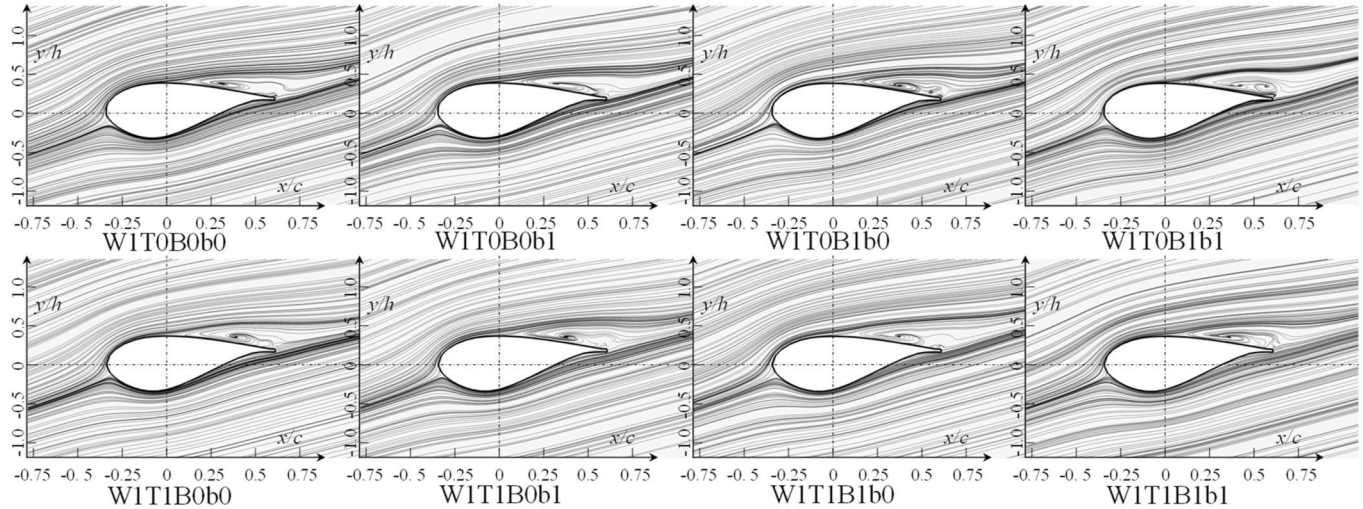

(b) at the 2/5 position

Fig. 27. Cross-sectional streamline on the blade root under turbulent inflow condition considering blade and tower flexibility.

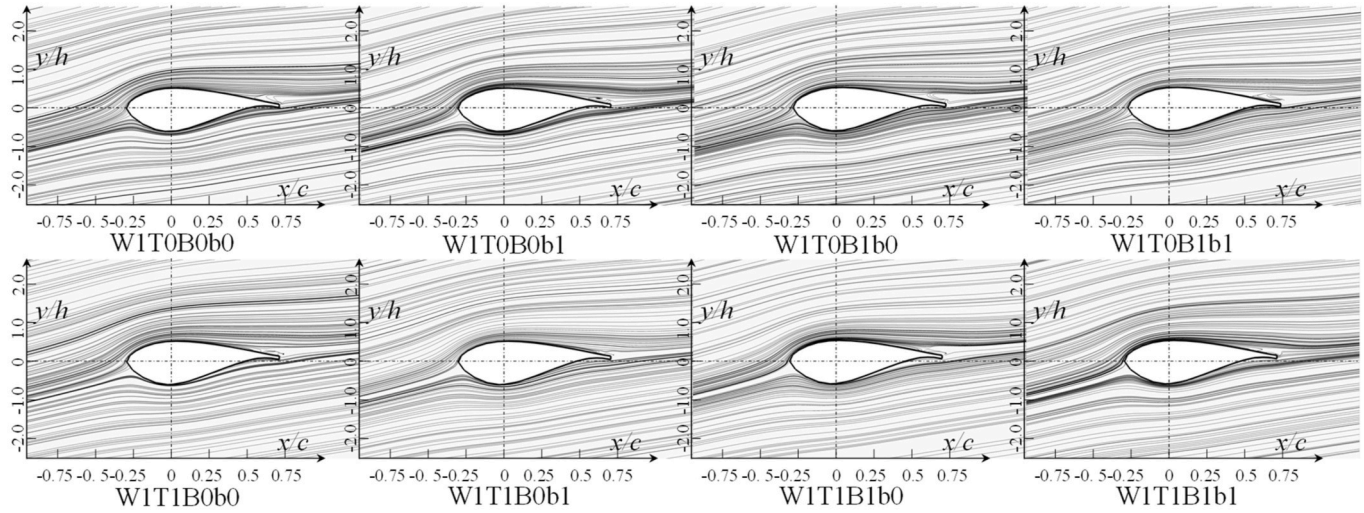

(c) at the 3/5 position

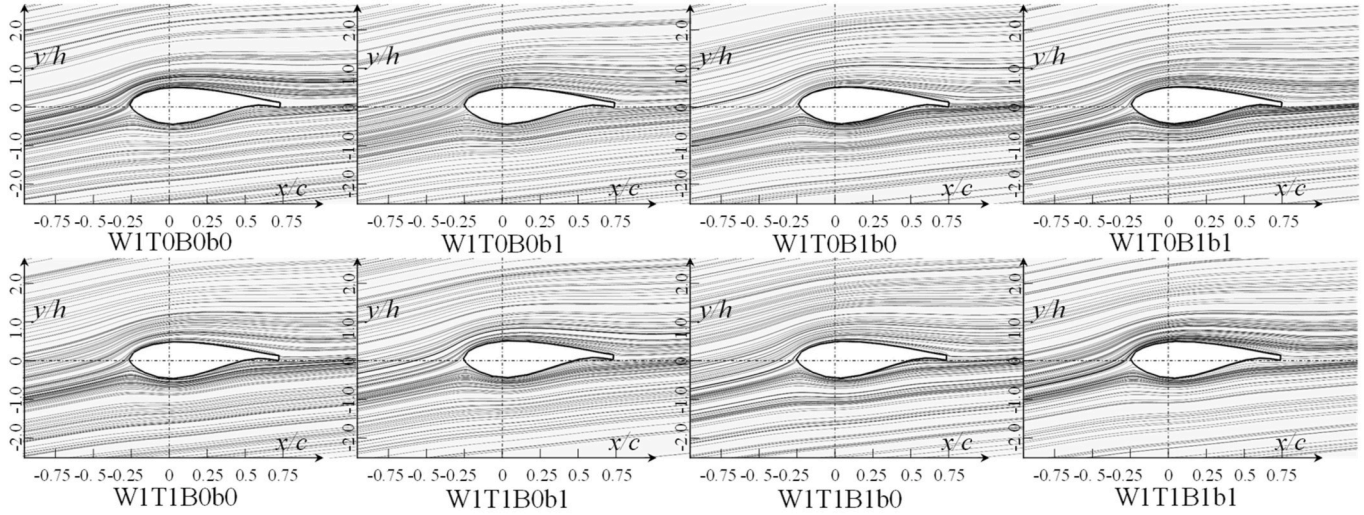

(d) at the 4/5 position

Fig. 27. (*continued*).

motion displays the smallest impact in Figs. 18 and 19. In turbulent winds, these differences are negligible due to frequent transverse energy exchange. However, as the wake develops, the peak value of the turbulence intensity profile gradually moves downwards in Fig. 20, with the turbulence intensity peak gradually shifting from blade tip to middle, eventually yielding the classic double-humped curve observed in Fig. 21.

3.4. Visualization of wake vortex

The wake vortex structures can be affected by different wind conditions, such as uniform or turbulent inflow. The inclination angle of each wake vortex can also be measured and studied, providing insights into the flow dynamics and revealing the influence of different factors, such as tower flexibilities and vertical inflow wind speed distributions. Understanding the role of vortices in the wake structure and flow dynamics of a wind turbine is crucial for optimizing wind turbine performance and enhancing the efficiency of wind energy generation.

This study employs the Q criterion for vortex identification and streamwise velocity for color mapping. Due to the disorderliness of wake vortices beyond x = 3D, this study only examines wake vortex structures in the 0~3D wake region. Wake vortex structures under uniform and turbulent wind conditions are presented in Figs. 22 and 23, respectively. Q value for uniform winds is 0.00002, while turbulent wind cases hold a Q value of 0.0007 due to ambient turbulence influence. It is observed that a more pronounced shedding of tip and root vortex under different wind conditions. Under uniform inflow conditions, the tip vortex stably develops without ambient turbulence or lateral kinetic energy until rupturing at downstream distance x = 3D. In the case of turbulent winds, due to more intense energy exchange in the flow field, the tip vortex ruptures at x = 0.5D and mixes with the incoming flow.

In addition, this study examines the inclination of wake vortices, determined quantitatively by measuring the inclination angle of the second-circle wake vortex structure, as illustrated in Fig. 22 through Fig. 25. Under uniform inflow conditions, the inclination angle ranges from 8° with a rigid tower to 9° with a flexible tower. Similarly, under turbulent inflow conditions, inclination angles increase to 10° and 11°, respectively. The inclination angle of the second-circle wake vortex

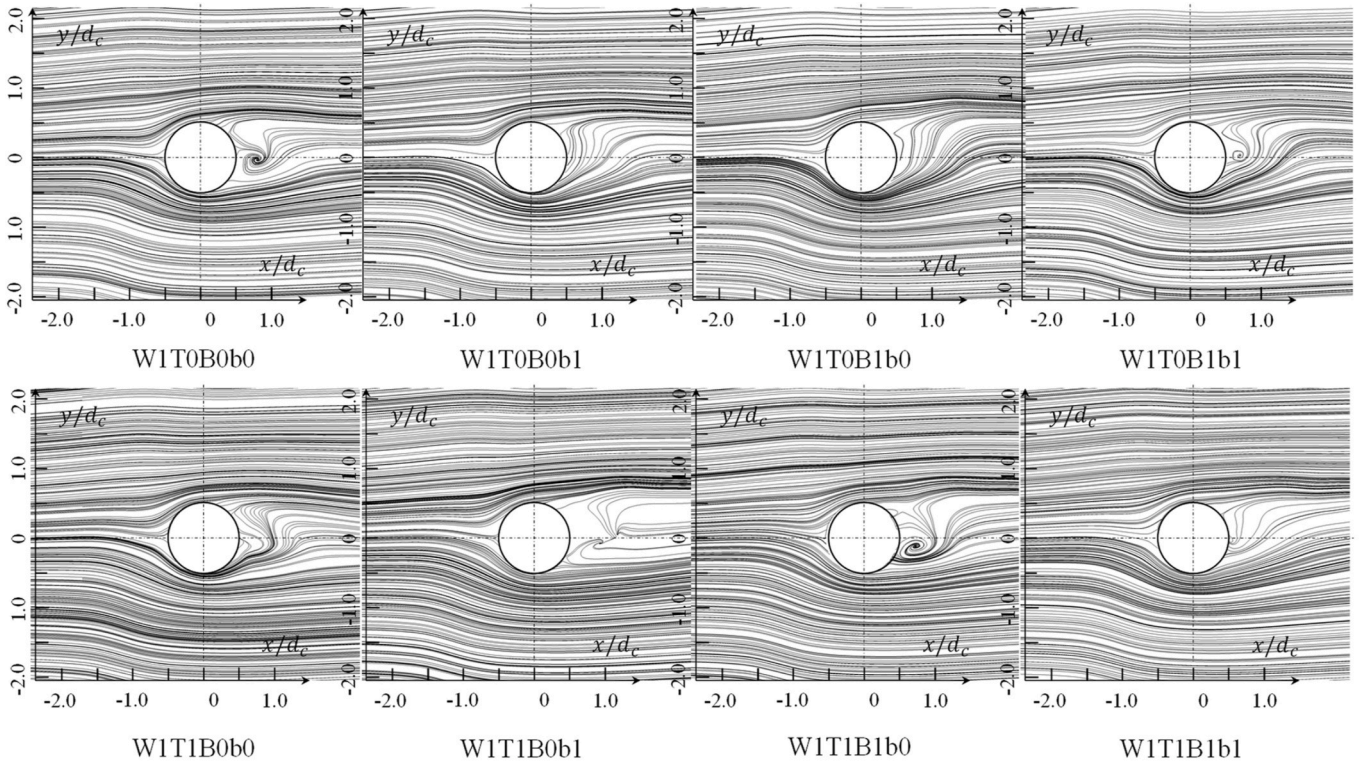

(a) under uniform inflow condition

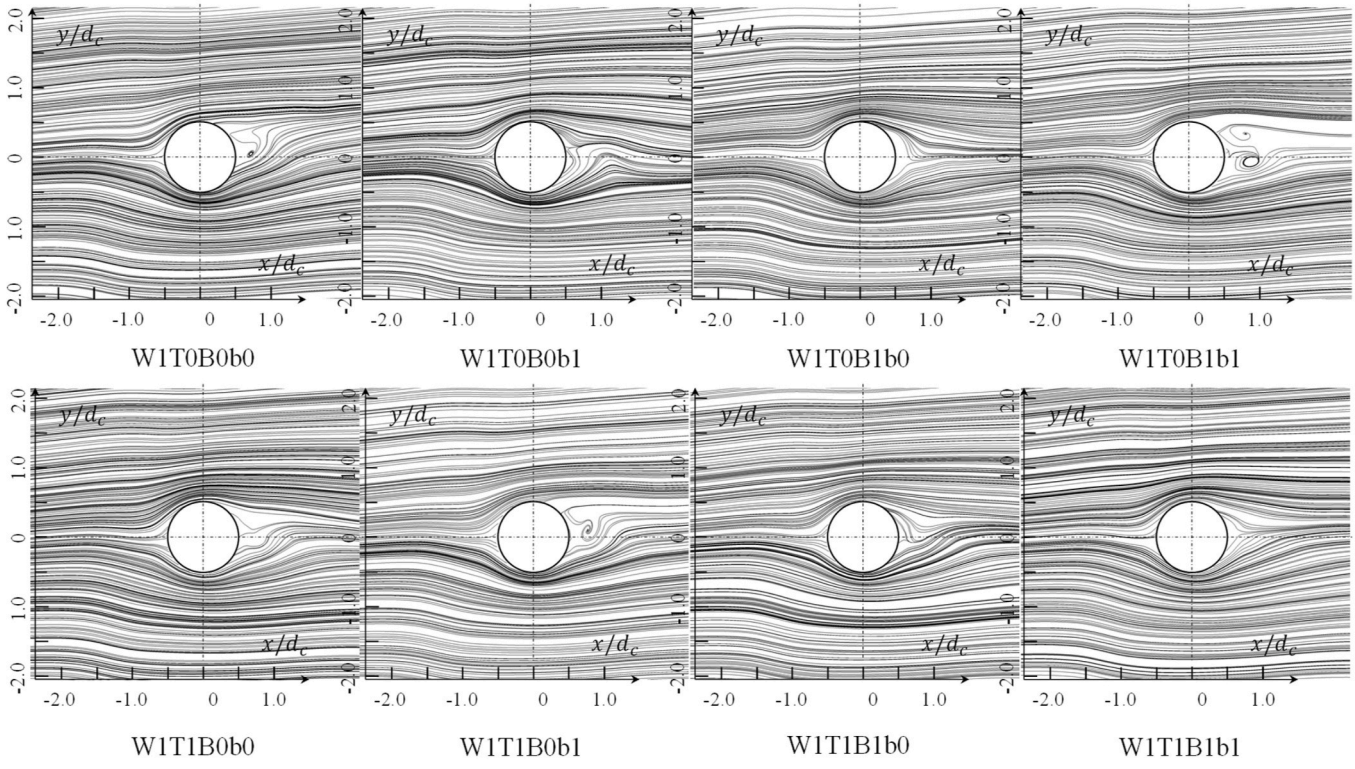

(b) under turbulent inflow condition

Fig. 28. Cross-sectional streamline on the tower at the blade tip height considering blade and tower flexibility.

structure for different cases are summarized in Table 5. Specifically, the inclination angle increases from 8° to 10° with the rigid tower when the inflow winds become turbulent. This value rises from 9° to 11° when it becomes flexible. The difference in tilt angles under different wind conditions is attributed to the fact that in turbulent wind conditions, the downwind wind speed increases with height, causing the wake vortex to be farther from the ground and its speed to be faster, resulting in a more uniform tilt angle under upwind wind conditions. Additionally, under uniform inflow conditions, the inclination angle changes from 8° to 9° when the tower becomes flexible, while under turbulent inflow conditions, this value changes from 10° to 11° in Figs. 24 and 25). This effect is caused by the elevation angle of the rotor rotation domain when the tower becomes flexible and the top of the tower moves.

3.5. Streamline on the blade and tower

The wake structure and flow dynamics in the wake region are significantly influenced by vortices on wind turbine blades and tower. As air passes over the curved surface of the blade, the shedding of tip and root vortices leads to the formation and evolution of wake vortex structures, which are responsible for the velocity deficit and added turbulent intensity observed in the wake region. These vortices cause a complex interaction between the wake and the air flowing over the blades. The streamlines are useful in the study of fluid mechanics phenomena such as turbulence, fluid separation, and vortex formation, therefore, the cross-sectional streamline diagrams at different positions are investigated. The cross-sectional streamline diagrams at the 1/5, 2/5, 3/5 and 4/5 positions from the blade root under uniform and turbulent wind conditions are presented in Figs. 26 and 27, respectively.

It is obvious that the flow separation occurs on the suction side of the blade with a small vortex and a large vortex near the blade root in Figs. 26(a) and Fig. 27(a) due to the smaller circumferential velocity and larger relative wind attack angle. It is also noted that the state of the two vortices on the suction side is different for the rigid and flexible tower conditions. When the tower is rigid, two stable vortices are formed, and vortex shedding does not occur. In contrast, for a flexible tower, it can be observed that the alternate occurrences of vortex shedding for the larger vortex occurs, while the smaller vortex remains stable. This phenomenon may be caused by the fact that the section displacement near the root is mainly affected by the tower vibration. When the tower is flexible, this section moves with the tower tip, and the spatial movement prevents the larger vortex from stably adhering to the blade surface, resulting in vortex shedding. This phenomenon exists under both uniform and turbulent wind conditions and is only related to the stiffness of the tower, which further demonstrates the importance of two-way fluid-structure interaction analysis. The merging of small and large vortices into a singular, larger vortex that is attached to the blade tailing edge occurs under both uniform and turbulent winds, as observed in Figs. 26(b) and Fig. 27(b). At the 3/5 positions, the vortex either moves towards the blade tailing edge or completely dissipates in uniform winds, as illustrated in Fig. 26(c), an observation entirely contingent on the flexibility of the blade and tower. Conversely, in turbulent winds, the vortex completely disappears for all cases, as confirmed by Fig. 27(c). At the blade tip in Figs. 26(d) and Fig. 27(d), which is the main working area, no flow separation occurs, and the airflow basically adheres to the blade surface, providing an effective torque to drive the blade rotation under both uniform and turbulent wind conditions.

Fig. 28 displays the cross-sectional streamlines around the tower at the blade tip position under different inflow conditions, taking into account blade and tower flexibility. It is worth noting that vortex shedding is fully developed for all cases under uniform inflow conditions in Fig. 28(a), indicating that blade and tower flexibility have little effect on the vortex shedding behind the tower. However, as the inflow conditions become turbulent, the vortex shedding phenomenon varies significantly with blade and tower flexibility. Specifically, when only the flap-wise motion of the blade is considered, the flow becomes an attached steady flow. Similarly, when all blade and tower flexibilities are considered, the flow also becomes an attached steady flow which may be caused by disturbance of the blades and tower. For other cases, the vortex shedding phenomenon can be observed behind the tower in Fig. 28(b).

4. Conclusions

This study mainly investigates the flow field characteristics in the wake region under both uniform and turbulent inflow conditions considering the blade and tower flexibility. Detailed investigations of the mean wind velocity, turbulent intensity, the wake vortices in the wake region and the streamline on the blade and tower have been conducted. The following conclusions are drawn.

1. The motions of blades and the tower have negligible effects on the mean wind velocity under both uniform and turbulent conditions while they significantly affect the turbulence intensity under uniform inflow conditions.
2. Under uniform inflow condition, the tower has the greatest influence on the turbulence intensity at the downstream distances with a maximum increase of approximately 45% in turbulence intensity (around the blade tip) when compared to the fully rigid case. The blade flap-wise motion has the second largest impact, increasing the maximum turbulence intensity by about 33% comparing with the fully rigid case.
3. The inclination of wake vortex is measured and quantitatively determined based on the inclination angle of the second-circle wake vortex structure. The inclination angles are 8° and 10° under uniform and turbulent inflow conditions for the fully rigid case due to the wind speed difference in the vertical direction. When the tower becomes flexible, these value increases to 9°–11° since the elevation angle of the rotor rotation domain varies when the tower becomes flexible and the top of the tower moves, respectively.
4. A large vortex and a small vortex are generated on the suction side near the blade root during the blade rotation. As the motion of tower is considered, the alternate occurrences of vortex shedding for the larger vortex occurs, while the smaller vortex remains stable. When all blade and tower flexibilities are considered, the flow around the tower becomes an attached steady flow which may be caused by disturbance of the blades and tower.

CRediT authorship contribution statement

Dongqin Zhang: Formal analysis, Software, Visualization, Writing – original draft, Writing – review & editing. **Zhenqing Liu:** Conceptualization, Funding acquisition, Methodology, Resources, Supervision, Writing – review & editing. **Weipeng Li:** Formal analysis, Investigation, Software, Validation. **Ling Cheng:** Supervision, Writing – review & editing. **Gang Hu:** Methodology, Writing – review & editing.

Declaration of competing interest

The authors declare that they have no known competing financial interests or personal relationships that could have appeared to influence the work reported in this paper.

Data availability

The authors do not have permission to share data.

Acknowledgements

This study was supported by National Natural Science Foundation of China (51978307).

References

Abdelsalam, A.M., Boopathi, K., Gomathinayagam, S., Hari Krishnan Kumar, S.S., Ramalingam, V., 2014. Experimental and numerical studies on the wake behavior of a horizontal axis wind turbine. J. Wind Eng. Ind. Aerod. 128, 54–65.

Ansys Inc, 2022. Fluent Theory Guide. Canonsburg, PA.

Bastankhah, M., Porté-Agel, F., 2014. A new analytical model for wind-turbine wakes. Renew. Energy 70, 116–123.

Bossanyi, E., 2003. GH Bladed Theory Manual. GH & Partners Ltd.

Cai, Y., Zhao, H., Li, X., Liu, Y., 2023. Effects of yawed inflow and blade-tower interaction on the aerodynamic and wake characteristics of a horizontal-axis wind turbine. Energy 264, 126246.

Carrión, M., Steijl, R., Woodgate, M., Barakos, G.N., Munduate, X., Gomez-Iradi, S., 2014. Aeroelastic analysis of wind turbines using a tightly coupled CFD–CSD method. J. Fluid Struct. 50, 392–415.

Couturier, P.J., Skjoldan, P.F., 2018. Implementation of an advanced beam model in BHawC. J. Phys.: Conf. Ser. 1037, 062015.

Dassault Systems, 2009. SIMPACK 2009 Simpack Assistant.

Della Posta, G., Leonardi, S., Bernardini, M., 2022. A two-way coupling method for the study of aeroelastic effects in large wind turbines. Renew. Energy 190, 971–992.

Dose, B., Rahimi, H., Herráez, I., Stoevesandt, B., Peinke, J., 2018. Fluid-structure coupled computations of the NREL 5 MW wind turbine by means of CFD. Renew. Energy 129, 591–605.

ElliotT, A.S., Wright, A.D., 1994. ADAMS/WT: an industry-specific interactive modelling interface for wind turbine analysis. The Energy-Sources Technology Conference. New Orleans, la, USA, pp. 111–122. Presented at the In:

Fu, S., Li, Z., Zhu, W., Han, X., Liang, X., Yang, H., Shen, W., 2023. Study on aerodynamic performance and wake characteristics of a floating offshore wind turbine under pitch motion. Renew. Energy 205, 317–325.

Gao, X., Li, B., Wang, T., Sun, H., Yang, H., Li, Y., Wang, Y., Zhao, F., 2020. Investigation and validation of 3D wake model for horizontal-axis wind turbines based on filed measurements. Appl. Energy 260, 114272.

Ge, M., Wu, Y., Liu, Y., Yang, X.I.A., 2019. A two-dimensional Jensen model with a Gaussian-shaped velocity deficit. Renew. Energy 141, 46–56.

Guo, N., Zhang, M., Li, B., Cheng, Y., 2021. Influence of atmospheric stability on wind farm layout optimization based on an improved Gaussian wake model. J. Wind Eng. Ind. Aerod. 211, 104548.

GWEC, 2022. Global Wind Report 2022.

Huang, G., Zhang, S., Yan, B., Yang, Q., Zhou, X., Ishihara, T., 2022. Thrust-matched optimization of blades for the reduced-scale wind tunnel tests of wind turbine wakes. J. Wind Eng. Ind. Aerod. 228, 105113.

Ishihara, T., Qian, G.-W., 2018. A new Gaussian-based analytical wake model for wind turbines considering ambient turbulence intensities and thrust coefficient effects. J. Wind Eng. Ind. Aerod. 177, 275–292.

Ishihara, T., Yamaguchi, A., Fujino, Y., 2004. Development of a new wake model based on a wind tunnel experiment. Global Wind Power.

Jensen, N.O., 1983. A Note on Wind Generator Interaction. Risø National Laboratory, Roskilde, Denmark.

Jonkman, J.M., Buhl, M.L., others, 2005. FAST User's Guide. National renewable energy Laboratory Golden, CO, USA.

Katic, I., Højstrup, J., Jensen, N.O., 1986. A simple model for cluster efficiency. In: European Wind Energy Association Conference and Exhibition, pp. 407–410.

Keane, A., 2021. Advancement of an analytical double-Gaussian full wind turbine wake model. Renew. Energy 171, 687–708.

Larsen, T.J., Hansen, A.M., 2007. How 2 HAWC2, the user's manual, tech. Rep. Risø-R1597. Risø National Laboratory, Technical University of Denmark, Roskilde and Kgs, Lyngby, Denmark.

Lee, H.M., Kwon, O.J., 2020. Performance improvement of horizontal axis wind turbines by aerodynamic shape optimization including aeroealstic deformation. Renew. Energy 147, 2128–2140.

Lee, K., Huque, Z., Kommalapati, R., Han, S.-E., 2017. Fluid-structure interaction analysis of NREL phase VI wind turbine: aerodynamic force evaluation and structural analysis using FSI analysis. Renew. Energy 113, 512–531.

Leng, J., Gao, Z., Wu, M.C.H., Guo, T., Li, Y., 2023. A fluid–structure interaction model for large wind turbines based on flexible multibody dynamics and actuator line method. J. Fluid Struct. 118, 103857.

Li, Y., Castro, A.M., Sinokrot, T., Prescott, W., Carrica, P.M., 2015. Coupled multi-body dynamics and CFD for wind turbine simulation including explicit wind turbulence. Renew. Energy 76, 338–361.

Li, Z., Gao, Z., Dai, Y., Wen, C., Zhang, L., Wang, J., 2023. Unsteady aeroelastic performance analysis for large-scale megawatt wind turbines based on a novel aeroelastic coupling model. Renew. Energy 218, 119370.

Li, Z., Wen, B., Dong, X., Peng, Z., Qu, Y., Zhang, W., 2020. Aerodynamic and aeroelastic characteristics of flexible wind turbine blades under periodic unsteady inflows. J. Wind Eng. Ind. Aerod. 197, 104057.

Lindenburg, C., 2018. Phatas User's Manual WMC. Wieringerwerf, the Netherlands.

Liu, Y., Xiao, Q., 2019. Development of a fully coupled aero-hydro-mooring-elastic tool for floating offshore wind turbines. J. Hydrodyn. 31, 21–33.

Liu, Y., Xiao, Q., Incecik, A., Peyrard, C., 2019. Aeroelastic analysis of a floating offshore wind turbine in platform-induced surge motion using a fully coupled CFD-MBD method. Wind Energy 22, 1–20.

Liu, Z., Fan, S., Wang, Y., Peng, J., 2021a. Genetic-algorithm-based layout optimization of an offshore wind farm under real seabed terrain encountering an engineering cost model. Energy Convers. Manag. 245, 114610.

Liu, Z., Peng, J., Hua, X., Zhu, Z., 2021b. Wind farm optimization considering non-uniformly distributed turbulence intensity. Sustain. Energy Technol. Assessments 43, 100970.

Liu, Z., Wang, Y., Nyangi, P., Zhu, Z., Hua, X., 2021c. Proposal of a novel GPU-accelerated lifetime optimization method for onshore wind turbine dampers under real wind distribution. Renew. Energy 168, 516–543.

Lopes, A.M.G., Vicente, A.H.S.N., Sánchez, O.H., Daus, R., Koch, H., 2022. Operation assessment of analytical wind turbine wake models. J. Wind Eng. Ind. Aerod. 220, 104840.

Miao, W., Li, C., Wang, Y., Xiang, B., Liu, Q., Deng, Y., 2019. Study of adaptive blades in extreme environment using fluid–structure interaction method. J. Fluid Struct. 91, 102734.

Muscari, C., Giordani, R., Schito, P., 2023. On wind turbine structural stiffness influence on wake flow. J. Fluid Struct. 118, 103862.

O'Brien, J.M., Young, T.M., Early, J.M., Griffin, P.C., 2018. An assessment of commercial CFD turbulence models for near wake HAWT modelling. J. Wind Eng. Ind. Aerod. 176, 32–53.

Øye, S., 1999. FLEX 5 User Manual. Danske Techniske Hogskole.

Piquee, J., García-Risco, A.Á., López, I., Breitsamter, C., Wüchner, R., Bletzinger, K.-U., 2022. Numerical investigations of a membrane morphing wind turbine blade under gust conditions. J. Wind Eng. Ind. Aerod. 224, 104921.

Porté-Agel, F., Wu, Y.-T., Lu, H., Conzemius, R.J., 2011. Large-eddy simulation of atmospheric boundary layer flow through wind turbines and wind farms. Journal of Wind Engineering and Industrial Aerodynamics, The Fifth International Symposium on Computational Wind Engineering 99, 154–168.

Qian, G.-W., Ishihara, T., 2019. Numerical study of wind turbine wakes over escarpments by a modified delayed detached eddy simulation. J. Wind Eng. Ind. Aerod. 191, 41–53.

Santo, G., Peeters, M., Van Paepegem, W., Degroote, J., 2019. Dynamic load and stress analysis of a large horizontal axis wind turbine using full scale fluid-structure interaction simulation. Renew. Energy 140, 212–226.

Sayed, M., Klein, L., Lutz, Th, Krämer, E., 2019a. The impact of the aerodynamic model fidelity on the aeroelastic response of a multi-megawatt wind turbine. Renew. Energy 140, 304–318.

Sun, H., Yang, H., 2018. Study on an innovative three-dimensional wind turbine wake model. Appl. Energy 226, 483–493.

Thangavelu, S.K., Chow, S.F., Sia, C.C.V., Chong, K.H., 2021. Aeroelastic performance analysis of horizontal axis wind turbine (HAWT) swept blades. Mater. Today: Proceedings, International Conference on Sustainable materials, Manufacturing and Renewable Technologies 47, 4965–4972, 2021.

Ti, Z., Deng, X.W., Yang, H., 2020. Wake modeling of wind turbines using machine learning. Appl. Energy 257, 114025.

Tian, L., Zhao, N., Wang, T., Zhu, W., Shen, W., 2018. Assessment of inflow boundary conditions for RANS simulations of neutral ABL and wind turbine wake flow. J. Wind Eng. Ind. Aerod. 179, 215–228.

Tian, L., Zhu, W., Shen, W., Zhao, N., Shen, Z., 2015. Development and validation of a new two-dimensional wake model for wind turbine wakes. J. Wind Eng. Ind. Aerod. 137, 90–99.

Uchida, T., Gagnon, Y., 2022. Effects of continuously changing inlet wind direction on near-to-far wake characteristics behind wind turbines over flat terrain. J. Wind Eng. Ind. Aerod. 220, 104869.

Wang, L., Quant, R., Kolios, A., 2016. Fluid structure interaction modelling of horizontal-axis wind turbine blades based on CFD and FEA. J. Wind Eng. Ind. Aerod. 158, 11–25.

Whale, J., Anderson, C.G., Bareiss, R., Wagner, S., 2000. An experimental and numerical study of the vortex structure in the wake of a wind turbine. J. Wind Eng. Ind. Aerod. 84, 1–21.

Wu, Y.-T., Porté-Agel, F., 2012. Atmospheric turbulence effects on wind-turbine wakes: an LES study. Energies 5, 5340–5362.

Xu, S., Zhuang, T., Zhao, W., Wan, D., 2023. Numerical investigation of aerodynamic responses and wake characteristics of a floating offshore wind turbine under atmospheric boundary layer inflows. Ocean Eng. 279, 114527.

Yang, K., Deng, X., 2023. Layout optimization for renovation of operational offshore wind farm based on machine learning wake model. J. Wind Eng. Ind. Aerod. 232, 105280.

Yassen, Y.ElS., Abdelhameed, A.S., Elshorbagy, K.A., 2023. An examination of hub wind turbine utilizing fluid-structure interaction strategy. Alex. Eng. J. 64, 1–11.

Ye, M., Chen, H.-C., Koop, A., 2023. Verification and validation of CFD simulations of the NTNU BT1 wind turbine. J. Wind Eng. Ind. Aerod. 234, 105336.

Yu, D.O., Kwon, O.J., 2014. Predicting wind turbine blade loads and aeroelastic response using a coupled CFD–CSD method. Renewable Energy, Special issue on aerodynamics of offshore wind energy systems and wakes 70, 184–196.

Zhang, D., Liang, Y., Li, C., Xiao, Y., Hu, G., 2022. Applicability of wake models to predictions of turbine-induced velocity deficit and wind farm power generation. Energies 15, 7431.

Zhang, J., Zhao, X., 2020. A novel dynamic wind farm wake model based on deep learning. Appl. Energy 277, 115552.

Zhang, R., Xin, Z., Huang, G., Yan, B., Zhou, X., Deng, X., 2022. Characteristics and modelling of wake for aligned multiple turbines based on numerical simulation. J. Wind Eng. Ind. Aerod. 228, 105097.

Zhang, S., Gao, X., Lin, J., Xu, S., Zhu, X., Sun, H., Yang, H., Wang, Y., Lu, H., 2023. Discussion on the spatial-temporal inhomogeneity characteristic of horizontal-axis wind turbine's wake and improvement of four typical wake models. J. Wind Eng. Ind. Aerod. 236, 105368.

Zhang, Z., Huang, P., Sun, H., 2020. A novel analytical wake model with a cosine-shaped velocity deficit. Energies 13, 3353.